Functional Oxide Depositions on Dielectric Substrates for Optical Applications

A THESIS SUBMITTED TO THE FACULTY OF THE UNIVERSITY OF MINNESOTA BY

Andrew D. Block

IN PARTIAL FULFILLMENT OF THE REQUIREMENTS FOR THE DEGREE OF DOCTOR OF PHILOSOPHY

Adviser Bethanie J.H. Stadler

November 2015

Abstract

Complex oxides of the transition metals are essential materials in the fabrication of photonic devices due to their high transparency in the infrared and the exotic properties they exhibit. Unfortunately, integrating them onto semiconductor platforms has proven to be a challenge due to significant differences in lattice constant (12-15Å compared to 5Å) and thermal expansion coefficient (~10^{-5} compared to 10^{-6}) leading to cracking in films during thermal processing. This work focuses on methods to integrate two complex oxides onto semiconductor platforms while minimizing crack formation and maximizing the optical properties used for photonic devices. The two oxides to be discussed are yttrium iron garnet (YIG), an oxide that exhibits the magneto-optical effect, and barium strontium titanate (BSTO), which exhibits the electro-optical effect. The discussion will begin with the fabrication procedures to make each oxide, focusing on the novel reactive sputter and rapid thermal anneal method used to achieve film crystallization. Film properties will then be discussed, including transparency, dielectric constant, and crystallization. Each of the two complex oxides exhibited extremely high photonic effects, magneto-optical for YIG and electro-optical for BSTO, respectively. From the work optimizing oxide thin films, methods to fabricate complex oxide waveguides were developed that resulted in high transparency and transmission of a guided mode. These materials are highly effective for use in semiconductor integrated photonics.

Contents

List of Tables

List of Figures

Chapter 1

Introduction

1.1 Communications Technologies

The field of digital communications has evolved from novelty to ubiquity to necessity in its 46-year lifetime since the inception of the Arpanet in 1969[5]. Currently 57% of Americans are owners of a smart phone, with that number expected to increase to 67% in as little as three years.[6]. There are currently 60 million users of Netflix, a streaming service that runs at a rate of 3Gb/hour[7]. Youtube is transmitting even larger volumes of data with a data rate of 35Mbps and over 1 billion users[8]. Driving and being driven by this trend has been an exponential expansion in data transmission rates comparable to and in fact surpassing Moore's law, doubling in transmission rates every 1.5 years, compared to the 2 years of transistor-doubling seen in semiconductors[9]. Forecasts predict that the next two decades will see a commensurate expansion, and IEEE is currently developing a new internet standard for 100Gb/s [10]. Such increases in data transmission will necessitate higher-bandwidth technologies.

Similar trends are being seen on the micro scale to those being witnessed on the macro scale. Processing speeds within CPU's are reaching the limitation of speed regulated by transmission line reflections along interconnects[11]. Electrical interconnects appear to

already be reaching their zenith both in high performance computing (HPC) and warehouse scale data-centers (WSD). Current HPC data systems are processing data at rates of 10^{16} FLOPS, with 10^{18} FLOPS necessary by the end of the decade, and WSD systems will require 1Tb/s data transfer rates between computers, exceeding the limitations of electrical interconnects[10, 12].

1.2 Photonics

Given the restrictions imposed by electrical interconnects, researchers are now envisaging a new medium of signal conduction, light, in a field called photonics. Optical signals have several advantages that make them a suitable choice for a new conduction mechanism. The frequency of a light wave is on the order of 10^{14}hz, and exploitation of a minimal fraction such as 1% of this bandwidth would lead to operation in the Thz range, facilitating the Tb/s data rates need for future HPC systems[13]. Additionally, the velocity of light is is considerably greater than that of electricity, and losses are less than those of electric transmission lines, making it useful for long-distance traversal as well as within datacenters[11]. Data transfer rates are not the only improvement provided by photonic systems. They also can use as little as 50 times less power to operate[10]. This has led to the implementation of photonics in the telecommunication market as a solution for problems for both short and long distances. Currently 10% of publicly traded company revenues are in the photonics industry[9].

1.3 Integrated Photonics

Much like to move to the integrated transistor, photonic systems are progressing towards on-chip devices to replace than those constructed in bulk. The field of nanophotonics involves the development of devices such as isolators and modulators that are monolithically integrated[12]. These devices could be utilized in combination with CMOS transistors, to

be used as interconnects, which will be able to push beyond the limits of wires, or they could eschew electronics entirely, having monolithically integrated networks using nothing but photons as the vehicle for signal conduction. New photonic innovations will impel the development of materials with enhanced optical properties to facilitate the same functionality as bulk counterparts with reduced optical path lengths.

1.4 Complex Oxides

Complex oxides are a class of materials possessing a multitude of properties that would be applicable for the augmentation of chip-scale photonic devices. While the exact definition of a complex oxide is disputable , the generally accepted definition is any oxide containing a transition metal and a group II element, generally in the perovskite structure. For the purposes of discussion, however, allowing structures other than perovskite, and other elements into the lattice, creates a definition comprising more materials, but still not departing from the term 'complex oxide.' Therefore the definition will be broadened to any oxides containing a transition metal and another element. This includes the perovskite structure, but there are many other complex oxides such as garnets or spinels that have exploitable properties. Complex oxides, like the transition metals of which they are composed, have a myriad of different compositions and properties, ranging from electro-optic, magneto-optic, piezoelectric, ferroelectric, and many others. Because of all of these exotic properties, many industries are interested in them for a wide array of applications including integrated photonics[14].

The benefits of complex oxides are numerous, but fabricating them and integrating them together with photonic materials is a challenge. As discussed in section 1.3, monolithically integrated electronics and photonics are made on semiconductor platforms, most frequently silicon, and the integration of complex oxides onto aforesaid platforms has been a venerable endeavor for materials scientists for several decades due to a high difference in thermal

expansion coefficients between complex oxides (~10^{-5}) and semiconductors (~10^{-6}). This leads to a high degree of stress during thermal processing, resulting in cracks in deposited films which scatter any transmitted light. For this reason, several different methods have been promoted to integrate complex oxides onto semiconductor platforms while minimizing thermal stress. These methods will be discussed in subsequent chapters.

1.5 The complex oxides in this Text

This thesis focuses on two high-transparency complex oxides with exotic optical attributes that can be exploited for integrated photonics. Prior to discussing them, chapter 2 introduces several of the fundamental experimental methods that were carried out in order to fabricate these materials, as well as computer simulations that were used to model their behavior and to design experiments.

The first material, to be discussed in chapter 3, is yttrium iron garnet (YIG), a material that exhibits the magneto-optical effect. An optimal process to make this material has been established prior to this text, so there will be a brief discussion and history on the procedure that has been used to make it. From this point, there will be a discussion on the new discoveries that were made, and how these discoveries led to a new YIG with the highest recorded magneto-optical effect in a thin film. The chapter will conclude with a description of future work and the direction of garnet research.

The second material, which will be discussed in chapter 4, is barium strontium titanate (BSTO), an electro-optic perovskite. Unlike YIG, the method used to make BSTO had not been fully been explored, so there will be special attention paid to the novelty of the method of this text and its ability to improve the fabrication process of BSTO, as well as the new considerations that must be taken with this deposition method. Also discussed will be the process to identify this material, as the characterization of the stoichiometry of BSTO is not conventional. This will be followed by a discussion on optical analyses and how the new

deposition method of this text allows for the fabrication of films of BSTO with extremely high electro-optic coefficients and high transparency.

Chapter 2

Experimental Methods, Lab Procedures, and Simulations

The two oxides that encompass this thesis were fabricated and characterized using a series of common lab techniques. Prior to delving into the nuances of each material severally, a comprehensive high-level overview of techniques and procedures for film deposition and analysis will be discussed in this chapter in order to establish the knowledge-base referenced in later in this text. Material specific procedures will be discussed their respective chapters.

2.1 Thermal Evaporation

Thermal evaporation consists of heating a material to its melting point in a vacuum chamber precipitating instantaneous evaporation resulting in vapor condensation onto the chamber and the sample. At high vacuum, impurities are reduced and the film has a highly uniform surface profile due to the linear travel path of the vaporized target molecules.

A diagram analogous to the process used for this research is shown in figure 2.1. The apparatus utilized contained an incandescent filament to heat the target material. The filament is made of tungsten due to its high melting point and resistivity. The filament has

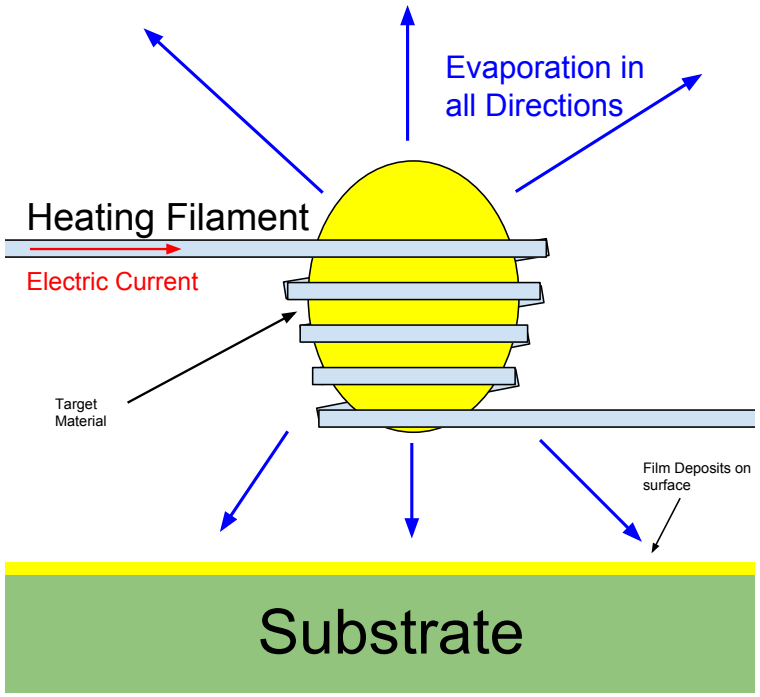

Figure 2.1: Diagram of thermal Evaporation

a coil in the middle, called the boat in which a pellet of the target material resides. It is crucial to reduce the pellet to a size of less them $2mm^3$ so that it does not act as a heat sink and prevent the filament from reaching a temperature sufficient for evaporation. At filament currents exceeding 20A, the boat produces a bright white glow and the target material rapidly sublimates, and its vapor coalesces into a film on the specimen. If the filament does not glow white, it is is not adequately hot. An increase in current will facilitate higher temperatures, but currents beyond 30A will sever the the filament, therefore it is recommended to reduce the pellet size rather than increasing current. Thermal evaporation was employed in this thesis for depositing metals with low melting points such as aluminum, silver, and gold.

2.2 Sputter Deposition

Sputtering is another vacuum deposition process that generates a different series of film properties than evaporation that is advantageous if those properties are preferred. In sputter deposition, a material is bombarded by the ions of a plasma and the target material is deposited onto the substrate surface to form a film. A diagram of the process is shown in figure 2.2. The stream of target particles begins at an apparatus called the *sputter gun*, which consists of the two electrodes needed to generate the plasma, and a gap between them called the glow. The target material acts as a cathode, which is usually in the shape of a circular disk, as was the case in the systems used in this thesis. Around the target is the anode, also called the *dark-space-shield.* During the deposition process, a noble gas, typically Ar, is flowed around the target forming into a concentrated vapor, which turns to a plasma upon ignition of the bias voltage between the electrodes. The now positively charged Ar ions are attracted to the negatively charged target with an electrostatic potential on the order of ~1keV, causing their collision with the target to impart enough kinetic energy into the target to induce the material to vaporize[1]. This vapor deposits onto the inside of the chamber and the substrate. The configuration shown in figure 2.2 is *sputter-up* configuration because the sputter gun faces upward, but an alternate *sputter-down* is also possible. Sputtering is useful in places where evaporation is prohibitively difficult, such as for metals with very high melting points such as tungsten. Sputtering also has the advantage of being a highly tunable process due to the multitude of process parameters, to be discussed in section 2.2.1, that can be adjusted, and with these widely varying process parameters, a profuse variety of materials can be deposited including metals, semiconductors, oxides, nitrides, and dielectrics. For this work, sputter deposition was used to make both complex oxide films.

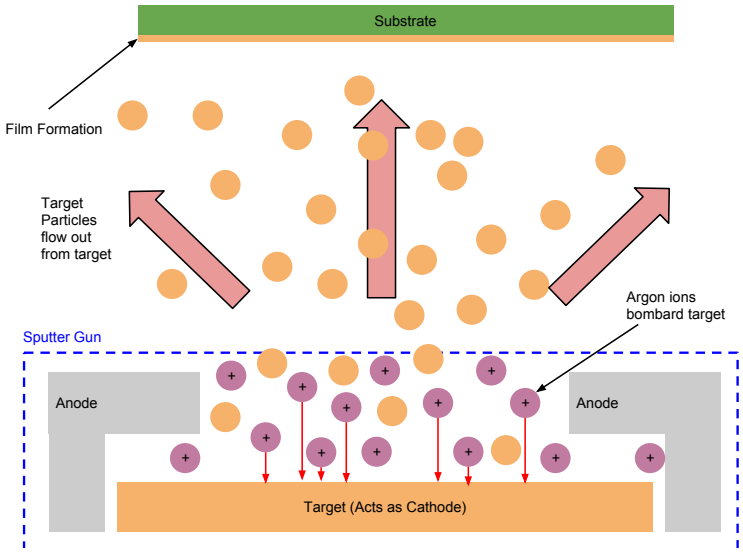

Figure 2.2: Diagram of Sputter deposition process

2.2.1 Deposition Parameters

2.2.1.1 Gas Pressure

The amount of argon used during a deposition has a significant effect on the deposition rate. When lighting a plasma, it is recommended to use as much argon as possible to ensure ignition. After lighting, there is an optimal amount argon to maximize deposition rate. Too little argon will result in reduced ion impingement on the target, while too much argon will interfere with the vapor and suppress deposition. The relation between Ar pressure and deposition rate consequently approximates an inverted parabolic curve as shown in figure 2.3. Ideal sputtering conditions are achieved at the top of this parabola where yield is maximized.

2.2.1.2 Applied Plasma Power

The main parameter that controls deposition rate is the amount of power in the plasma being used to sputter the target. The sputter deposition rate is linear with applied plasma power by the equation:

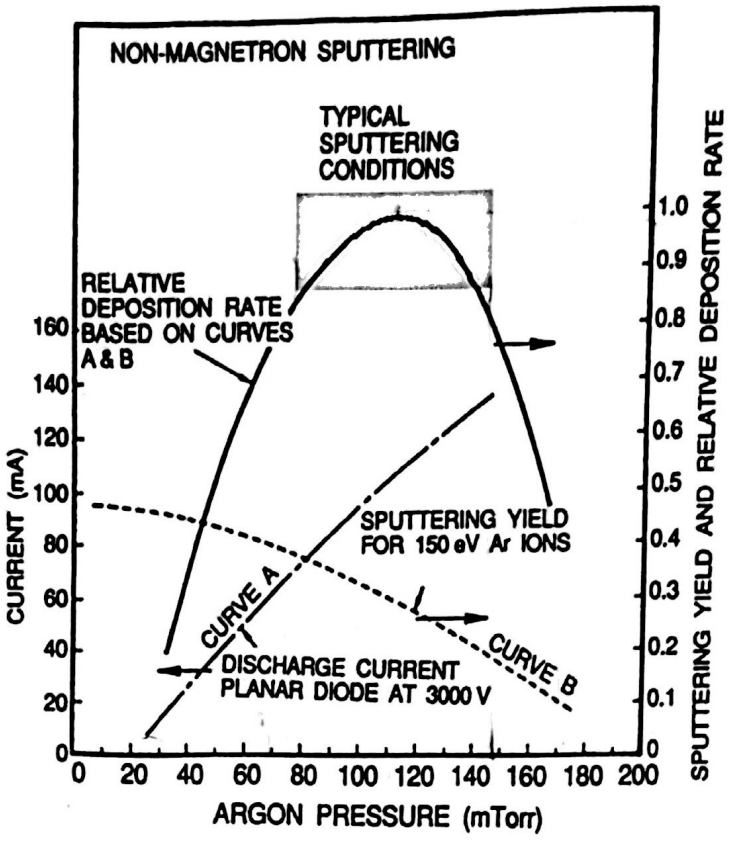

Figure 2.3: Sputter yield as a function of Ar pressure[1].

$$S = \frac{3\alpha 4 M_1 M_2 E}{4\pi^2 (M_1 + M_2)^2 U_S} \tag{2.1}$$

where S is the sputter yield, M_1 and M_2 are the respective masses of the Ar ions and target atoms, E is the ion energy, U_S is the target sublimation energy, and α is a constant ranging from .1 to .4[1]. Note that $S \propto E$ meaning that increases in plasma power will directly correlate to increases in deposition rate.

From equation 2.1 it is apparent that maximizing plasma power results in higher deposition rates. However, it is not always advisable because the plasma generates a substantial amount of heat, and materials with low melting points will melt if the applied power to them is too high. In particular, bismuth should not have a power beyond 30W applied to it, and alloys of gallium, tin, and indium also have the risk of melting. It is also important to take the bias voltage into consideration when sputtering. While there is not a precise standard on what the bias voltage should be, if the bias goes beyond 800V, the material is most likely too insulative or magnetic to sputter.

2.2.2 Magnetron Sputtering

In order to increase ion collisions into the target, most sputtering systems use magnetrons to assist them. A magnetron is a magnet placed behind the target, with its magnetic flux facing perpendicular to the plane of the target. Under the influence of the magnetron, the equations of electron motion are defined by

$$y = -\frac{q\varepsilon(1 - \cos\omega_c t)}{m_e \omega_c^2}$$

$$x = \frac{\varepsilon t}{B}\left(1 - \frac{\sin\omega_c t}{\omega_c t}\right)$$

where ω_c is the cyclotron frequency of the electron[1].This results in the electron trajec-

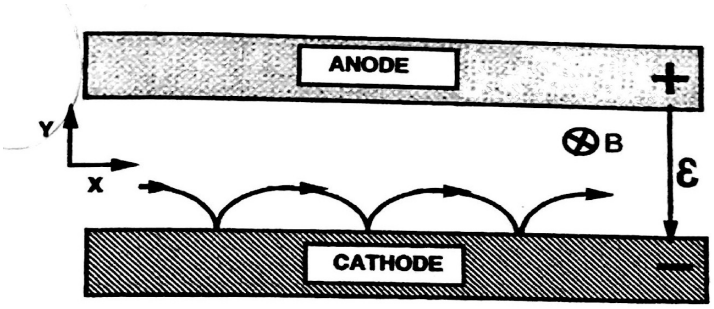

Figure 2.4: Electron trajectory in a magnetic field[1]

tory shown in figure 2.4. This results in longer electron lifetimes and maximizes ionizing efficiency at the target and improved plasma density[1].

For magnetic materials such as iron, it important to use very high strength magnetrons in order to focus as much magnetic flux as possible into the plasma. It is also necessary to make magnetic targets as thin as possible to reduce the amount of flux in the target and ensure that all of the magnetic flux is in the plasma. For iron, the limit of thickness is 1/16 of an inch, but for alloyed targets, the target can be thicker.

2.2.3 RF and DC sputtering

For conductive targets such as metals, current will conduct directly through the target and maintain a stable plasma. This is known as DC sputtering. For materials that are not effective conductors , DC sputtering is not possible. In these circumstances, the plasma is modulated by an rf pulse so that it will not terminate. This is referred to as rf sputtering. rf sputtering is used for the deposition of insulators such as ceramics or for sputter deposition in a reactive environment as will be discussed in section 2.2.5.

2.2.4 Co-sputtering

There are two procedures that can be employed for the formulation of alloy or compound films. One method is the implementation of a composite target, since many material suppliers have alloying or sintering services and can make targets to specifications if there is a

Figure 2.5: Three lit plasmas. The blue is titanium, the green is barium, and the purple is strontium. The variation in colors are related to the ionization energies of each metal. Besides being visually appealing, the plasmas also give a visual indication of their state. A pink color in the plasma is an indication of surface oxidation, therefore an effective way to tell if pre-sputter is complete is to visually examine the plasma color.

limit on the number of guns in the sputtering chamber or if a very exact composition is required fer every film. The alternative to single composite target sputtering is co-sputtering, in which multiple targets are ignited and deposit simultaneously, shown in the photograph of figure 2.5. Equation 2.1 has already shown the linear relation between the plasma power and the relative deposition rate of a materials, so making a specific formulation of an alloy is possible, and co-sputtering has the advantage of being capable of tuning film stoichiometry independent of target composition., but there are several variables to take into consideration when co-sputtering which will be discussed in detail in sections 4.6 and 4.7.

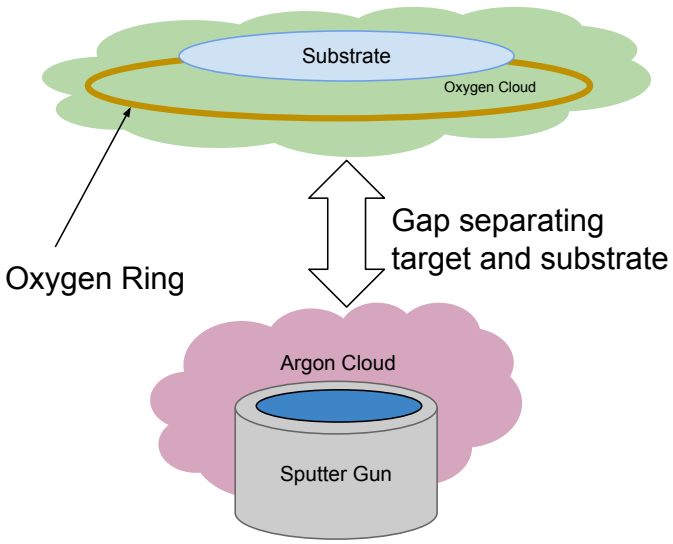

Figure 2.6: Reactive Sputtering

2.2.5 Reactive sputtering

Compound ceramic films can be deposited by use of ceramic targets or they can be fabricated by reactive sputtering, in which metal targets are sputtered in a reactive environment to create a compound film. A diagram of the way this process was performed is shown in figure 2.6. In reactive sputtering, a reactive gas such as oxygen is flowed around the substrate and reacts with the target particles to form a compound film on the substrate surface. The ring shown in figure 2.6 is perforated with holes which inject gas to surround the sample. This ring is kept in close proximity the substrate and away from the target to prevent the reactive gas from causing the target to oxidize and inhibit ignition of the plasma. Some gas will still reach the sputter gun, and for metals that readily oxidize, reactive sputtering must use an rf power source instead of DC.

2.3 Rapid Thermal Anneal

Oxide films require annealing to overcome their crystallization enthalpy. This, however, must be done under the constraint that the films do not crack due to thermal stress as

discussed in section 1.4. Rapid thermal annealing (RTA) systems employ infrared lamps to heat samples. This allows samples to be heated at rates of 100-150C^{o}/s, which reduces annealing time, reaching crystallization temperatures in a mater of seconds, minimizing the thermal budget and mitigating the risk of crack formation.[15]. RTA also allows for the addition of gasses during the anneal such as oxygen to fill oxygen vacancies or react with the film to produce an oxide.

2.4 Chemical Vapor Deposition

The fabrication processes that have been discussed thus-far are referred to as *physical vapor deposition* processes because the target material is physically changed in order to be deposited onto the surface of the substrate. This is in contrast to *chemical vapor deposition* (CVD), in which a precursor material undergoes a chemical reaction as it deposits onto the substrate. In CVD, a precursor gas such as SiH_4 is flowed into a chamber and chemically reacts according to the following equation:

$$SiH_4 + O_2 \longrightarrow SiO_2 + H_2$$

to produce a film of silica[1].

CVD is performed at low pressures (~100mTorr) and high temperatures (~700^{o}C) in a process called low-pressure CVD (LPCVD). In order to reduce this temperature, a plasma can be ignited inside the deposition chamber. This is referred to as plasma enhanced chemical vapor deposition (PECVD)[1, 15]. PECVD films tend to be less dense than LPCVD films, therefore LPCVD films are used for etch masking rather than PECVD films. PECVD also do not adhere to substrates as well as LPCVD films, an effect which will be discussed later in section 4.17.

2.5 Atomic Layer Deposition

Atomic layer deposition (ALD) is a form of chemical vapor deposition that uses precisely timed infusions of precursor to produce high-quality films of materials. These stepes of the process are ordered according to the arrangement of figure 2.7. The surface of a wafer is chemically behaves according to figure 2.7a with dangling OH bonds extending from it as a result of exposure to atmosphere. The precursor is then introduced, shown in figure 2.7b, using methyl aluminum as an example. This precursor reacts with the surface, breaking the methyl bonds and creating an aluminum oxide surface layer and methane product gas, shown in figure 2.7c. The product is then vacuumed out and water vapor is introduced into the chamber as shown in figure 2.7d. The water reacts with the methyl bonds, forming new OH bonds for another layer of aluminum oxide to attach to. The final step is shown in figure 2.7e, in which the process is complete and a layer of Al_2O_3 is now formed on the surface.

An immediate question comes to mind: how is the ALD process distinct from CVD? The difference is that CVD is a process of continuous gas flow, and the chemical reaction that occurs is continuously occurring on the surface of the wafer. By contrast, ALD is a cyclical process, requiring specialized microvalves to inject the precursor gas quickly enough to perform.

It may seem from the depictions of figure 2.7 that ALD is a monolayer or epitaxial process. In actuality, there will still be defects in the film, and the film generally does not end up growing as a single crystal. Nevertheless, ALD does grow highly textured films that are very dense, and is useful for growing thin dielectric films.

2.6 Reactive Ion Etching

Reactive ion etching (RIE) involves a low energy chemically reactive plasma to etch a material. In RIE, a reactive gas such as CHF_3 is flowed into a chamber with the sample,

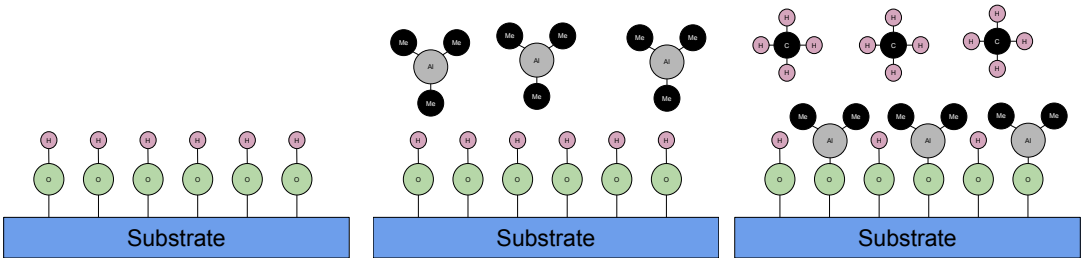

(a) Surface of Wafer Prior to ALD (b) Introduction of precursor gas (c) Reaction With surface to form oxide layer

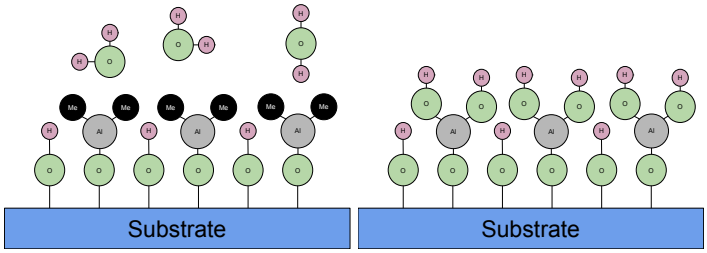

(d) Introduction of water into process chamber (e) Completion of ALD cycle leaves new dangling OH bonds. These bonds form new attachment points for the next cycle of methyl aluminum.

Figure 2.7: ALD Process

usually mixed with Ar to increase conductivity. A voltage is then applied to the gas to induce a plasma, and the energized F^+ ions bombard the surface of the sample, chemically reacting with the surface to remove deposited material.

The mechanics of RIE are very similar to those of sputtering in that the process involves ions bombarding a surface to remove material. The difference in RIE is that the fluoride ions are chemically reactive and are removing material mostly by a chemical process. If pure argon were used to physically remove material, the process would be known as *ion milling*, which is effective for removing materials that are chemically inert, but due to the high impact energies of argon ions, the process tends to leave small craters in the material as it etches, making it difficult to use for nanoscale devices. RIE tends to mitigate this effect, but it still can occur as will be shown in section 4.17.2.

2.7 X-ray Diffraction

The primary method for determining the crystal structure of a material is X-ray diffraction (XRD). In order to understand the physics behind XRD, it is instructive to consider the difference between X-rays and light and how it affects an X-ray's interaction with matter. Imagine shining a laser beam on a highly reflective surface like a silicon wafer. At any given angle, the laser will reflect off of the surface of the sample at the same angle in which it hit the wafer, and no matter what angle the laser hits the surface, it will reflect off and a beam will be visible coming off the sample. This is because the light waves are significantly larger than an atomic spacing, and the the light interacts with the surface of the sample as if that surface is continuous.

Now instead consider an X-ray beam incident a silicon wafer. Unlike a light wave, the wavelength of an X-ray is of the same order of magnitude as an atomic spacing. Thusly when an X-ray interacts with the wafer, it is not interacting with a continuous surface, but a discrete series of atoms. These atoms will interact with the X-ray to induce a phase shift

and form a diffraction pattern. The phase shift will be related to the incident angle of the X-ray. If the phase shift of the X-ray is such that constructive interference occurs, X-ray reflections will be visible and will appear, otherwise they will not. Therefore for any given material, the atomic lattice can be characterized by scanning the surface of the sample across a spectrum of angles with the X-ray beam. The angles of constructive interference will appear as peaks in a diffraction spectrum.

The locations of the peaks in the diffraction spectrum are defined by the well known Bragg's law . Bragg's law says that for an incident angle θ of X-rays, the position of the maxima in the spectrum will be where $2d\sin(\theta) = n\lambda$ where d is the atomic spacing and n is an integer multiple of the wavelength of the X-ray. Values for n are typically between 1 and 3 depending on the size of the unit cell.

Two derivations for Bragg's law are included in this thesis. The first is based on geometry and ray tracing, and is more well-known. There is a second derivation based on free space diffraction. It is not as familiar, but is somewhat less mathematically rigorous and is more intuitive to those familiar with diffraction theory, therefore it will be included as well.

2.7.1 The Geometric Solution to Bragg's Law

To derive Bragg's law, consider the diagram shown in figure 2.8a, which shows planes of atoms, and an incident X-ray shown as a ray. The X-ray traverses two paths, first with the top layer of atoms, forming path $\overline{AD}$, and the second path below it, $\overline{ABC}$. In order for there to constructive interference at angle , it must be the case that:

$$\overline{ABC} - \overline{AD} = n\lambda$$

Meaning that the phase difference between the two paths must be exactly one wavelength apart. These distances can be related to the atomic planar spacing by the following equations:

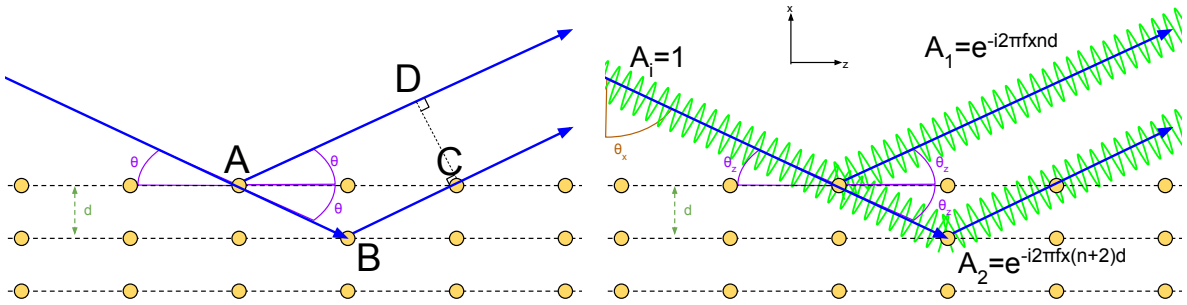

(a) Diagram of XRD for geometric derivation of Bragg's law

(b) Diagram of XRD for Optical Derivation

Figure 2.8: Graphics of the Derivations of Bragg's Law

$$d = \overline{AB}\sin(\theta) \Rightarrow \overline{AB} = d/\sin(\theta) \Rightarrow \overline{BC} = d/\sin(\theta) \Rightarrow \overline{ABC} = 2d/\sin(\theta)$$

$$d = \frac{\overline{AC}}{2}\tan(\theta) \Rightarrow \overline{AC} = 2d/\tan(\theta)$$

It can also be observed that:

$$\overline{AD} = \overline{AC}\cos(\theta)$$

Substituting these equations yields the following result:

$$\overline{AD} = \overline{AC}\cos(\theta) = \frac{2d}{\tan(\theta)}\cos(\theta) = 2d\frac{\cos(\theta)}{\sin(\theta)}\cos(\theta) = \frac{2d\cos^2(\theta)}{\sin(\theta)}$$

This can then be brought back into the initial equation:

$$n\lambda = \frac{2d}{\sin(\theta)} - \frac{2d\cos^2(\theta)}{\sin(\theta)} = \frac{2d}{\sin(\theta)}(1-\cos^2(\theta)) = \frac{2d}{\sin(\theta)}\sin^2(\theta) = 2d\sin(\theta)$$

The final equation results in Bragg's law[16].

2.7.2 The Optical Solution to Bragg's Law

While the solution for Bragg's law from section 2.7.1 is relatively intuitive from a geometric perspective, it is rather complex, and there is a simpler solution using free space diffraction. Consider the diagram from figure 2.8b which depicts the X-rays as angular plane waves. The incident plane wave is shown as A_i and the two diffracted plane waves are $A_1$and A_2. For any given position of n lattice spacings into the crystal, the two plane angular plane waves can be represented by the following set of equations:

$$A_1 = Ae^{-\iota(2\pi f_x nd)}$$

$$A_2 = Ae^{-\iota(2\pi f_x (n+2)d)}$$

Where f_x represents the spatial frequency of the angular plane wave in the x direction. The $(n+2)$ factor in the calculation of A_2 comes from its traversal across another lattice spacing, forward and backward, just as in section 2.7.1. Factoring the equation for A_2 gives the following result:

$$A_2 = Ae^{-\iota(2\pi f_x (n+2)d)} = Ae^{-\iota(2\pi f_x nd + 4\pi f_x d)}$$

This reveals that A_2 is actually a phase shifted version of A_1. Since A_1 and A_2 must interfere constructively, the phase shift of A_2 must be equal to 2π. Therefore:

$$4\pi f_x d = 2\pi n$$

$$2f_x d = n = 2d\frac{\cos(\theta_x)}{\lambda} = 2d\frac{\sin(\theta_z)}{\lambda}$$

$$2d\sin(\theta_z) = n\lambda$$

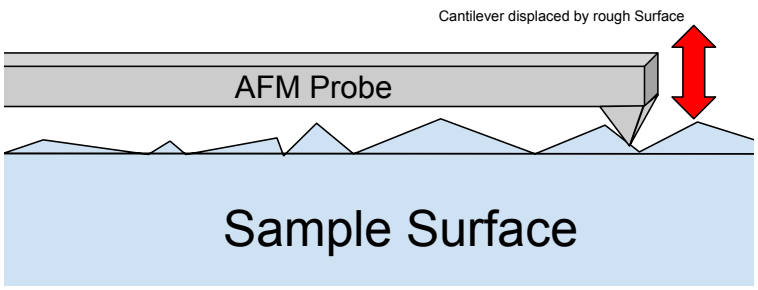

Figure 2.9: Diagram of AFM process

which is Bragg's law.

2.8 Surface Profilometry

A common technique for establishing film thickness is *profilometry*. Profilometry consists of using a probe to scan across the surface of a film and measure the height of features as it scans. Thickness with the profilometer consists of performing a liftoff with the deposited film. Prior to the deposition, the substrate is marked with a polymer to mask off a region for liftoff. After deposition, sonication in acetone will remove the polymer and deposited film, creating a step which can be scanned by the profilometer. As well as being an effective method for determining film thickness, it can be used to characterize the contours of patterned structures or measurement of surface roughness.

2.9 Atomic Force Microscopy

Atomic force microscopy (AFM) is similar to profilometry but uses a much finer probe tip to precisely scan the surface of a film or structure. A diagram of the process is shown in figure 2.9. The tip of the AFM is typically made out of silicon and is fabricated using an anisotropic chemical etch, resulting in an atomically sharp tip and very high precision. AFM is useful for measuring the surface topology of films to view grain structure and cracks, and is also useful for establishing the shape of devices such as waveguides.

2.10 Ellipsometry

Ellipsometry is an optical technique that can measure the thickness and index of a film using a laser or spectral light source. From electromagnetics, it is known that the electric field in a light wave is modeled as two sine waves, E_{TE} and E_{TM}, with a phase delay between. If the phase delay is 0^o, the wave is linearly polarized. if the phase delay is 90^o, the light will be circularly polarized. If the phase is another value, the light will have some measure of ellipticity to it. Ellipsometry measures the difference in ellipticity of an incident wave on the surface of a film to the wave reflecting off of it. The reflection coefficient of the film ρ is defined by:

$$\rho = \frac{r_{TE}}{r_{TM}} = \frac{E_{TERef}/E_{TEInc}}{E_{TMref}/E_{TMInc}} = \tan\psi e^{i\Delta} \tag{2.2}$$

Different values of ρ are then fit to different theoretical models to determine film thickness and index[1]. Ellipsometry is capable of measuring film thickness down to the atomic layer, making it a very effective characterization technique. The one challenge of ellipsometry is the fact that it does not directly measure a specific film property, and instead requires computerized curve-fitting based on models to calculate properties. Occasionally it is possible that the computer models do not fit with experiment, particularly when multiple layers of a film are present. Still the method is very reliable and useful for measuring the optical properties of thin films.

2.11 Stoichiometric Compositional Analysis Methods

One of the things that was somewhat overlooked in section 2.7 was this question: from where do the X-rays originate in the first place? The theory behind this question correlates very well with stoichiometric analysis techniques, so a brief discussion on X-ray generation will be enlightening. When a high energy electron collides with a material, it excites an

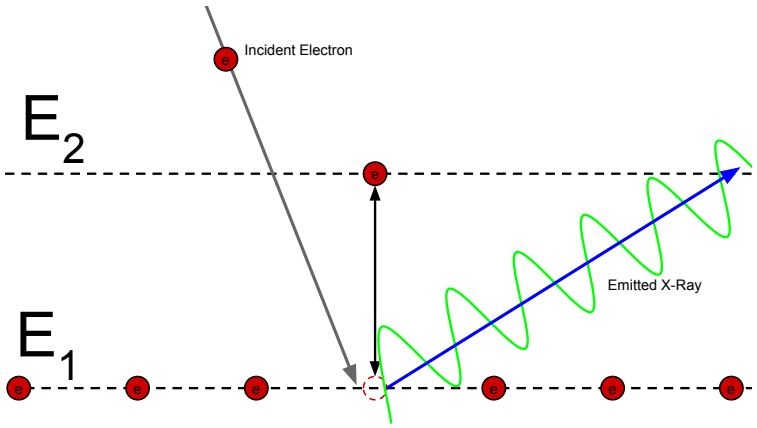

Figure 2.10: Diagram of transitions in a material

electron in the material to a higher energy state. This is shown in figure 2.10 in which an incident electron energizes one of the electrons in the material from E_1 to E_2. When the electron descends from E_2 back into E_1, it will release energy, usually in the form of an X-ray[1]. Every element has a characteristic X-ray spectrum that it emits. XRD is constructed by Cu disk an electron beam and generating 1.54Å X-ray.

Because the X-ray emission pattern is unique for any given element, the stoichiometry of a material can be determined by bombarding it with electrons and measuring its X-ray spectrum[17, 1]. There are two analysis methods that exploit this phenomenon. Energy dispersive spectroscopy (EDS) measures the X-ray energy using a semiconductor detector. Wavelength dispersive spectroscopy (WDS) takes the emitted X-rays and diffracts them using a crystal. Because the lattice spacing of the crystal is fixed and known, the variability of the diffraction pattern will come from the X-ray spectrum emitted by the material. EDS is a simpler process to perform, requiring nothing more than an electron source and a detector. WDS is a more involved process, requiring calibration to a standard every time a measurement is performed, however the results of WDS are more accurate and the process is useful when exact stoichiometry is required or when the FWHM-overlap in the spectrum of EDS are within the spectral resolution of the instrument.

2.12 Numerical Simulations

Waveguide devices and photonic structure were simulated using numerical methods prior to fabrication. The software used for simulation was Lumerical FDTD Solutions. This software uses the finite difference time domain (FDTD) method to solve photonics problems and simulate the performance of photonic devices. The FDTD method divides time into Δt regions and space into Δx regions defined by $\Delta t = \Delta x/(2c_0)$ and computes them according to finite element computation[18]. Lumerical FDTD uses the FDTD method to solve Maxwell's equations and derive performance of photonic structures. Specific discussion of simulation results will be discussed in sections 3.14 and 4.17 .

2.13 Conclusion

Several different fabrication and characterization methods were employed to make complex oxides for this text, and this chapter has surveyed them in some detail. In particular this chapter focused on sputter deposition because that has been the preponderance of production in making the oxides in this text. In addition, supporting techniques were discussed, and they should be illuminating to the reader in developing a base of knowledge that will guide them on their further research into complex oxides.

Chapter 3

Yttrium Iron Garnet Films for Magneto Optical Applications

3.1 Optical Isolation

In an optical system, it is integral that reflections along the optical path do not reflect back into the laser source. Such reflections can cause instability or even damage to lasers. For this reason, the first component in the system after the source laser is an optical isolator. An isolator is a device that will allow light to propagate through it in only one direction, with light reflecting back in the opposite direction being blocked by the isolator.

3.2 Yttrium Iron Garnet

Yttrium iron garnet (YIG) is a material that is almost exclusively used in the fabrication of isolators. The garnet structure is space group 230, $Ia\bar{3}d$ and the chemical formula of $A_3B_2C_3O_{12}$ where the A atoms occupy 8-coordinated dodecahedral sites, the B atoms occupy 6-coordinated octahedral sites, and the C atoms occupy 4-coordinated tetrahedral sites. In YIG, both the tetrahedral and octahedral sites are occupied by Fe^{3+} ions and the dodecahedral site is occupied by a Y^{3+} ion, for a formula of $Y_3Fe_5O_{12}$. The unit cell of

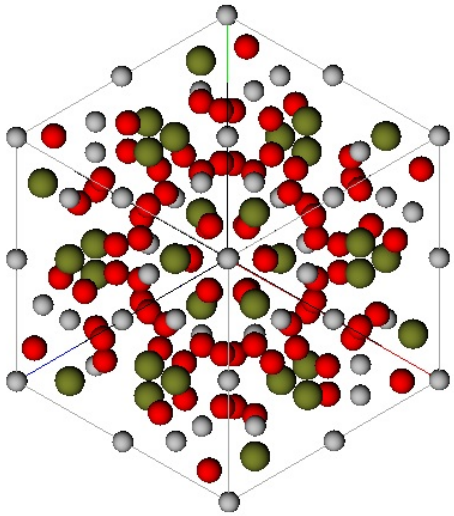

Figure 3.1: Crystal Structure of Yttrium iron garnet shown facing the (111) axis

YIG is shown in figure 3.1. The YIG lattice contains 64 transition metal cations and 96 oxygen anions and has a lattice constant of 12.376Å.

3.2.1 Magnetic Properties

Due to the Fe atoms in YIG, it is ferrimagnetic. A ferrimagnetic material is an oxide containing iron atoms antiferromagnetically coupled to another transition metal by super-exchange through the oxygen atoms in the lattice, and due to an imbalance in the antiferromagnetic coupling, the material exhibits a net magnetic moment. A good example of ferrimagnetic magnetization is the spinel ferrites. A spinel contains 8 tetrahedral sites and 16 octahedral sites, resulting in a spin imbalance between the tetrahedral and octahedral sites as shown in table 3.1 using nickel ferrite as an example[1].

By contrast, YIG has a more complex unit cell, containing not just the 8 tetrahedral sites and 16 octahedral, but an additional 24 dodecahedral sites. Consequently, the spins

[1]Nickel ferrite is not in fact a material that exists in a normal ferrite phase, only in the inverse phase. This example is for demonstration purposes only.

Spinel Type	A Site	B Site 1	B Site 2	Net Magnetization (μ_B)
Normal Spinel	Ni^{2+}	Fe^{3+}	Fe^{3+}	
Magnetization (μ_B)	2	5	5	2
Direction	$\rightarrow$	$\leftarrow$	$\rightarrow$	
Inverse Spinel	Fe^{3+}	Ni^{2+}	Fe^{3+}	
Magnetization (μ_B)	5	2	5	2
Direction	$\rightarrow$	$\leftarrow$	$\leftarrow$	

Table 3.1: Spinel Ions and spin moments

	A Site	B Site 1	B Site 2	C Site 1	C Site2	C Site 3	Net Magnetization (μ
Atom	Y^{3+}	Fe^{3+}	Fe^{3+}	Fe^{3+}	Fe^{3+}	Fe^{3+}	
Magnetization (μ_B)	0	5	5	5	5	5	5
Direction	0	$\leftarrow$	$\rightarrow$	$\leftarrow$	$\rightarrow$	$\leftarrow$	

Table 3.2: Garnet Ions and spin moments

will take the form of table 3.2. All spins cancel except for one of the tetrahedral sites, creating a net magnetic moment in YIG.

3.2.2 Birefringence and the Magneto-optical Effect

In crystalline materials, the index of refraction can be anisotropic. The index tensor is defined by :

$$n = \begin{bmatrix} n_x & 0 & 0 \\ 0 & n_y & 0 \\ 0 & 0 & n_z \end{bmatrix} \tag{3.1}$$

If a linearly polarized plane-wave is traveling along either the x,y, or z axis with its electric field along one of the other axes, it will maintain its polarization as it passes through the material[19]. For example, if the light is propagating along the z axis and its electric field is along x or y , it will remain linearly polarized. However, when the electric field is not precisely on one of the perpendicular axes of the crystal, such as the electric field is a combination of components of x and y, its polarization state will be rotated as it passes through the material[19]. This is shown in figure 3.2, showing a polarization rotating as the

light propagates. When this condition is met, the index tensor takes the form of equation 3.2.

$$n = \begin{bmatrix} n_x & 0 & \imath n_{xz} \\ 0 & n_y & 0 \\ \imath n_{xz} & 0 & n_z \end{bmatrix} \tag{3.2}$$

In the majority of materials this index tensor is symmetric and as a result, light that passes through this material will exhibit *time reversal symmetry*. Time reversal symmetry can be understood by considering what happens after the light passes through the media and reflects back through it. In a time-reversal symmetric material, the polarization rotation of the light will always be symmetric along the propagation direction. Figure 3.3a shows what will occur. As light passes back through the material in the other direction, it's polarization rotation will still be the same direction relative to its propagation direction, which is now the opposite of its original propagation direction. Because of this, light that passes back through the material will have the same polarization as it started with when it entered the material.

In magnetic materials, the Zeeman interaction between the radiation and the media induces a polarization rotation, known as the *magneto-optic effect*. When light is reflecting off of a magnetic material like a metal, it is referred to the *magneto-optical Kerr effect* (MOKE) . When light is transmitting through a transparent magnetic material, it is called the Faraday effect.

In a magneto-optic material, the index tensor is defined by equation 3.3. The anti-symmetry of magnetization produces a correspondingly anti-symmetric tensor. Because of this, a reflected wave traversing back through the material is now no longer parallel to the magnetization, but anti-parallel to it. This causes the polarization rotation to go in the opposite direction relative to the magnetization, or the same direction relative to the original propagation direction of the light. This is shown in figure 3.3b in which the reflected

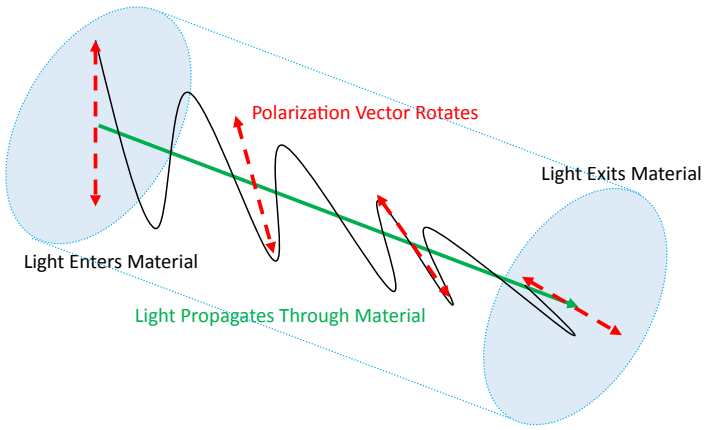

Figure 3.2: Polarization rotation through a birefringent material

wave continues to rotate the same direction. When the reflected light reaches it's original position, it will have rotated by twice the amount that it rotated as it passed through the magnetic material.

The polarization rotation in a magnetized material is defined by $\theta_F = l\theta_v \vec{M} \cdot \hat{D}$ where θ_F is the amount of total Faraday rotation, l is the length of material being traversed, $\vec{M}$ is the magnetization of the material, $\hat{D}$ is the propagation direction of the light, and θ_v is the intrinsic Faraday rotation of the material, called the *Verdet constant.* The units of the Verdet constant are degrees/length/magnetization, and typically the value is given in literature as degrees/cm at saturation.

$$n = \begin{bmatrix} n_x & 0 & \imath n_{xz} \\ 0 & n_y & 0 \\ -\imath n_{xz} & 0 & n_z \end{bmatrix} \tag{3.3}$$

3.2.3 Non Reciprocal Phase Shift

When light is guided through a waveguide such as an SOI ridge waveguide the guided mode will experience a phase shift. In TM guided modes, the phase shift is induced by a cladding placed on top of the the guiding material, while for TE guided modes, the magneto-optical cladding is deposited adjacent to the waveguide[20]. Because the magneto-optical layer is

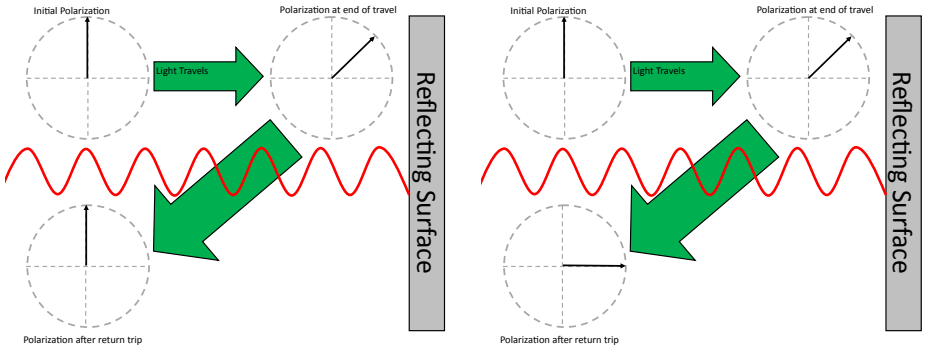

(a) Time-Reversal-Symmetric Media (b) Non-Time-Reversal-Symmetric Media

Figure 3.3: Reflection in Birefringent media

non-reciprocal, the phase shift will also be non-reciprocal, meaning that it will have the opposite phase shift if the light is guided in the opposite direction through the waveguide[21].

3.3 Optical Isolation Using the Magneto-Optical Effect

Optical isolation and non-reciprocal materials are closely related. There are two methods by which non-reciprocal materials can be exploited for optical isolation.

3.3.1 Using Rotation

The Faraday effect can be used to construct an isolating device directly. The structure consists of two polarizers with the magneto-optical material sandwiched between them. The two polarizers are set 45^{o} out of alignment and the length of magneto-optical material is engineered such that the light will be rotated by 45^{o}. When the light hits the first polarizer, it is polarized and then passes through the magneto-optical material into the second polarizer, where it passes through. Any light that is reflected back is rotated by another 45^{o}, and will be 90^{o} out out alignment with the input polarizer after its full traversal. It is thusly blocked by the input polarizer and will not enter back into its laser source.

An isolator is shown in figure 3.4. These are bulk devices fabricated by liquid phase epitaxy using a gadolinium gallium garnet (GGG) substrate. When an optical system is set

up, this isolator must be placed directly after to the laser source to prevent back-reflections . The aforementioned bulk isolator is only usable in optics bench scale systems. As was alluded to in section 1.3, in order to scale an isolator to a chip-scale platform, methods will have to be developed to both monolithically integrate YIG, and increase its magneto-optical performance to be able to achieve isolation in a reduced path length. This will be the further focus of this chapter.

3.3.2 Using Non-Reciprocal-Phase-Shift

For monolithically integrated devices, the isolator is being integrated with silicon photonics, and this means that light is going to need to be guided in a silicon waveguide. This is more conducive to devices based upon non-reciprocal phase shift. One method that has been proposed is to build a Mach-Zehnder interferometer (MZI) and then perturb one branch of the MZI with a YIG layer[20]. Another approach has been to deposit a YIG layer onto a silicon ring-resonator, which will have a different resonance condition in one direction than in the reverse direction[22]. Both approaches have advantages and disadvantages, and currently it is undetermined which design will be the better one.

3.4 Semiconductor Integration

Integrating YIG into semiconductor platforms has posed many challenges due to an extraordinary dissimilarity between garnets and semiconductor materials. Bulk isolators have been fabricated on other garnets such as gadolinium gallium garnet (GGG). Since GGG is a garnet, it is possible to epitaxially lattice match to it, leading to higher transparency and magneto-optical effect. On silicon, the lack of a lattice matching surface induces the formation of other yttrium oxides and iron oxides rather than the garnet phase. This is an even greater problem when attempting to substitute other elements into the garnet layer. Elements such Ce and Bi will enhance the magneto-optical effect, but they have a very high

tendency to form into other oxides rather than the garnet phase. Also the thermal expansion coefficient of YIG ($1.04 * 10^{-5}$) is much higher than that of silicon ($2.6 * 10^{-6}$) so there will be large amount of thermal stress at the interface between the film and the substrate leading to cracking in films. Several methods were attempted to circumvent this problem, such as epitaxially growing YIG on GGG and then wafer bonding to silicon[23], or in some cases using a thin layer of adhesive to bond the two layers together[24].

Extensive research has gone into developing a method to grow YIG directly on silicon without having to resort to overly unconventional tricks such as adhesive bonding. Within the past decade, a method was developed using sputter deposition and RTA to grow garnet films on silicon substrates. Separate metal Y and Fe targets were sputtered in the presence of a flow of oxygen to form an amorphous film with the stoichiometric ratio of Fe:Y of 5:3. The film was crystallized by RTA in oxygen. It was found that by establishing the correct stoichiometric ratio of Y to Fe, and inundating the sample with large amounts of oxygen during thermal processing to fill vacancies, the garnet phase would readily form. This represented a great breakthrough in the integration of YIG with semiconductors because it was the first time garnet had been successfully grown directly onto silicon[25].

While it may initially seem that all the problems have now been solved, there were still challenges associated with the sputter deposition of garnet. First, there is still large amount of film stress present, especially during the annealing step. This results in the formation of micro-cracks which dramatically decrease the transmission of the deposited films. Secondly, while YIG itself was grown on silicon, pure YIG is in fact not sufficient for monolithic integration due to the fact that it does not have that large of a Verdet constant by itself. In order to get a large enough magneto-optical effect to scale an isolator to a chip, the garnet must be substituted with Ce or Bi, which will substitute into the lattice at the Y sites, increasing the Faraday effect. These substituted garnets, however, are much more resistant to formation into the garnet phase, and using the same deposition method to deposit them resulted in the formation of bismuth oxides and cerium oxides as previously discussed.

3.4.1 Engineering of Thermal Expansion Stress

Stress in a film is going to be directly proportional to the expansion of a film. Consider the following:

$$\frac{\partial L}{L} \propto \partial T$$

$$\frac{\partial A}{A} \propto 2\partial T$$

$$\frac{\partial V}{V} \propto 3\partial T$$

The increase in thermal expansion of a material will be directly proportional to the dimensionality of the film. Therefore by reducing or eliminating any dimension in the film, a commensurate dramatic reduction in film stress will result making it possible to suppress the formation of cracks. Depositing ultra-thin films would reduce the out-of plane-dimension, and photolithographic patterning would effective at reducing the in-plane dimensions. Both of these methods were attempted by different research groups to explore their effects.

3.4.2 Waveguide patterning

One of the approaches to the problem of thermal expansion is to reduce the length or width of garnet layers to prevent thermal stresses in garnet films. This is achieved by patterning the garnet layer using photolithography and etching prior to annealing, then when the film is annealed, its surface area is reduced, and the films do not crack. YIG films were sputter deposited, then they were patterned by photolithography into waveguides with widths from 0.7m to 2.0m. The waveguides were etched using phosphoric acid, then they were annealed for crystallization. The YIG waveguides did not crack and were highly transparent in the

Figure 3.4: Industrially Fabricated Optical Isolator[2]

infrared[26].

3.4.3 Thin YIG Films

Another alternative in reducing the volume of YIG used in the deposition is to reduce the thickness of films of YIG. These films should form into the garnet phase without cracking because of a reduction of the volume of YIG. Ross et. al experimented with this method by depositing 20nm YIG layers onto semiconductor substrates[27]. The extremely reduced dimensions mitigated cracks and films formed into the garnet phase. Furthermore, because these films were made of YIG, they would allow for lattice matching of another garnet deposited on top of them, acting as a *seed layer* for the growth of the second layer of garnet. The second layer would then be substituted with Ce or Bi for enhanced magneto optical effect[22]. This technique was then integrated with an SOI ring resonator to make an isolator based on non-reciprocal phase shift[22].

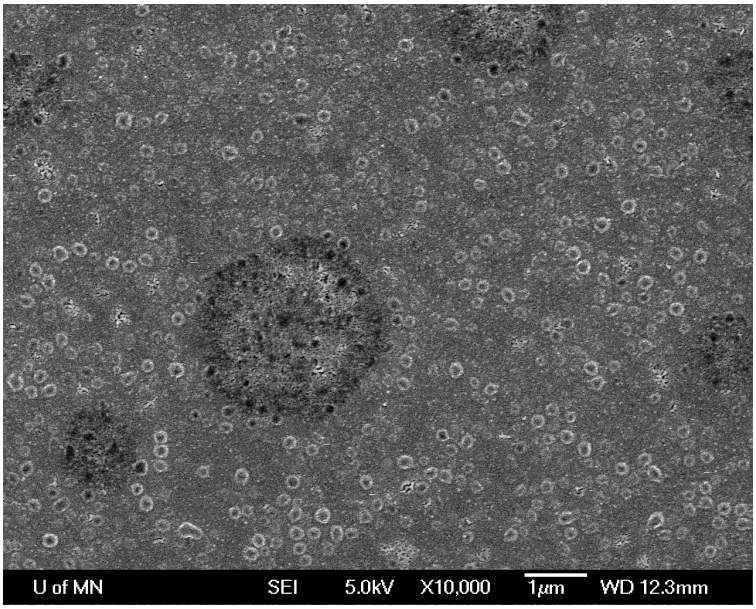

Figure 3.5: YIG film annealed at 850°C. It contains many cracks and bubbles.

3.5 Replication of Ross et. al

The thin-film work in section 3.4 represented the state-of-the-art in YIG integration with semiconductors prior to the research in this text. To further the knowledge of this research area, both of the methods of sections 3.4.2 and 3.4.3 were explored. The first part of this project was to attempt to recreate the results of [27]. To do this, the sputtering procedure from section 3.4 was used. Targets of Fe and Y were sputter deposited in an atmosphere of oxygen and then crystallized by rapid thermal anneal. The Fe target had a plasma power of 220W and the Y target had a plasma power of 140W. The argon flow rate was 20sccm and the oxygen flow rate was 2.0sccm. Films were deposited for short periods of approximately 5 minutes and films were shown to be approximately 30nm thick by profilometry. Films were annealed at temperatures ranging from 800°C to 850°C. All of the films crystallized, however, films annealed at 850°C had formed bubbles and cracks as shown in figure 3.5. Because of this, all further films were annealed at 825°C as this was found to be the temperature limit before films would experience formation of bubbles.

All films indicated the presence of the garnet phase after anneal and no other phases

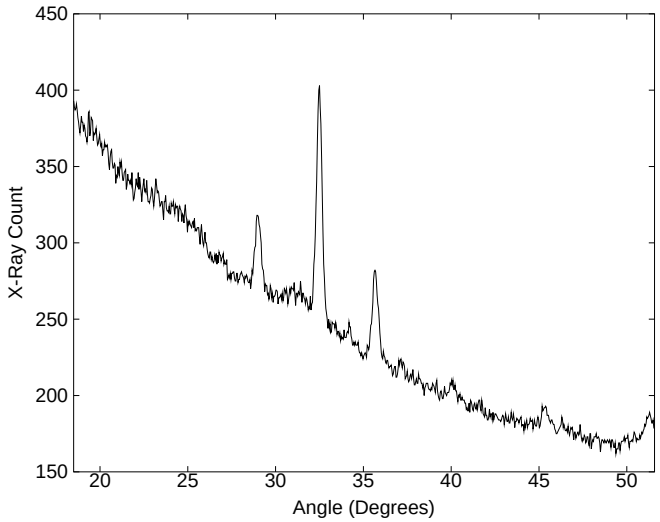

Figure 3.6: XRD results for typical YIG films. Patterns are consistent with YIG phase[3].

were present. Typical XRD spectra, shown in figure 3.6, are consistent with the YIG phase. From this data, it would seem that the attempt to duplicate the results of [27] were successful.

3.6 Discovery of a Problem

Further inspection by microscopy was used to examine films for cracks. Cracks were not found, but another discovery was made. While the XRD results indicated the exclusive presence of YIG, upon inspection with visible light microscopes and scanning electron microscopes (SEM), the films do not look homogeneous. Figure 3.7 shows typical film appearance in an SEM. The films are not composed of a single phase, but in fact consist of a series of spots and a surrounding matrix. It was initially believed that this was caused by a lack of cleanliness in the substrate, but more thorough cleaning procedures were used which did not eliminate this problem.

Due to the absence of any other phases in the XRD pattern, it was reasonable to consider that the spots in the films were grains of YIG, and the surrounding matrix had remained amorphous. To confirm this hypothesis, a process called *electron backscatter diffraction*

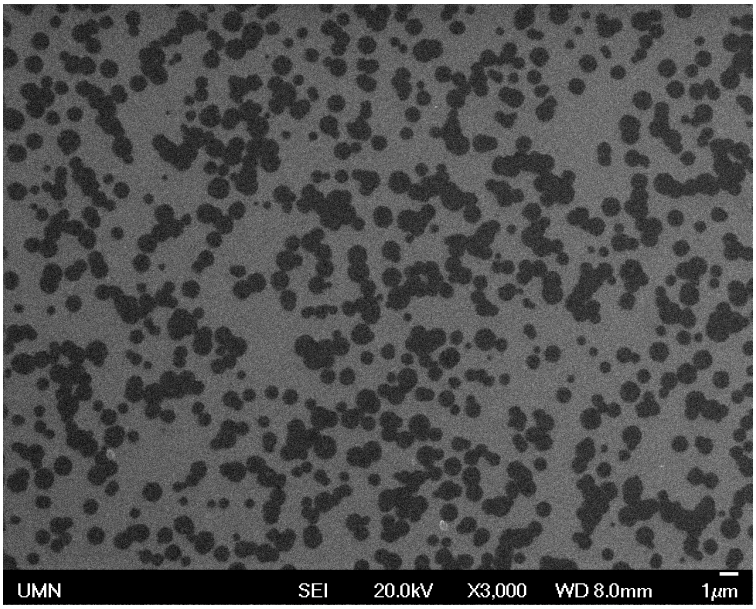

Figure 3.7: Typical thin film of YIG after annealing. Notice that the film has formed into two phases.

(EBSD) was used to examine the microstructure of the YIG films. EBSD is the process of performing diffraction, similar to XRD, with the electron beam from the SEM. The electrons will diffract according to Bragg's law, and will produce a unique aerial diffraction pattern which can be used to identify the crystal structure of the films. Because the electron beam is focused, it is possible to hit individual crystallites with it and produce single crystal patterns rather than the aerial rings of XRD. This allows the user to identify many different characteristics about the crystallinity of the film, such as grain orientation, grain size, and how grains form boundaries against one another. The 30nm YIG films were examined by EBSD, and and the results are shown in figure 3.8. To understand the figure, consider the legend in the upper right corner. Each of the cubic crystal orientations is represented by a different RGB value. Red is $\{100\}$, green is $\{110\}$ and blue is $\{111\}$. Any region that shows up in color in the image is therefore crystalline, with an RGB value corresponding to its orientation, and the gray region corresponding to amorphous or unidentified material. The image confirms that the spots in the films are crystal grains surrounded by an amorphous matrix. Each of the grains shows up in a different color, indicating that they

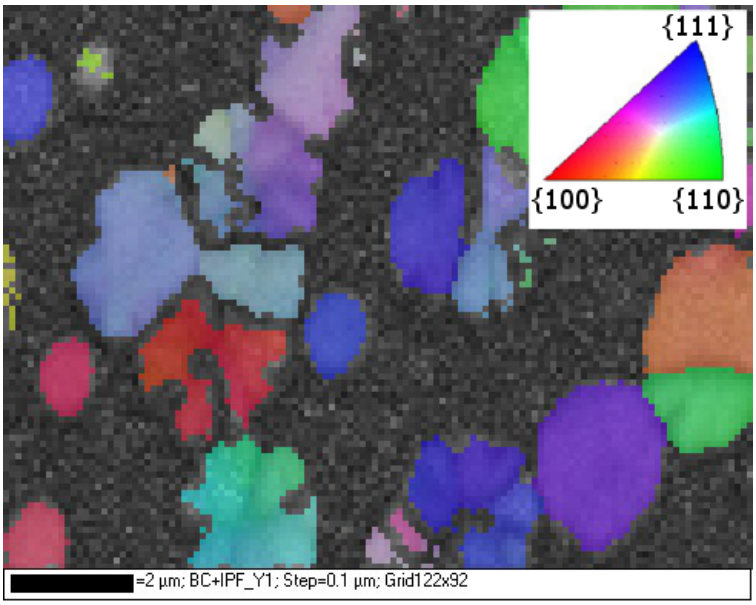

Figure 3.8: EBSD image of YIG films[3]

do not crystallize with any preferred orientation. This is consistent with the XRD results indicating films were polycrystalline.

This was a surprising result. Previous results from [27] and [22] indicated that complete crystallization of YIG films was possible, however the results that were obtained did not exactly corroborate this. the supplemental material of [22] did say, however, that magnetic measurements of films indicated that they were only partially crystallized. This presented a new challenge: is it possible to achieve full crystallization of YIG thin films so that they can be used as seed layers, leading to even greater magneto-optical effect?

3.7 Discovery of a Solution

After the initial examinations of section 3.5, further research was conducted to more precisely tune the parameters of YIG deposition. One of the first parameters to explore was deposition rate, and in these experiments, a fortuitous phenomenon was discovered. A sintered Y_3Fe_5 target was sputtered with a power of 200W using an rf plasma and 1.9sccm of oxygen and enough argon to produce a chamber pressure of 6.0mtorr. Under these con-

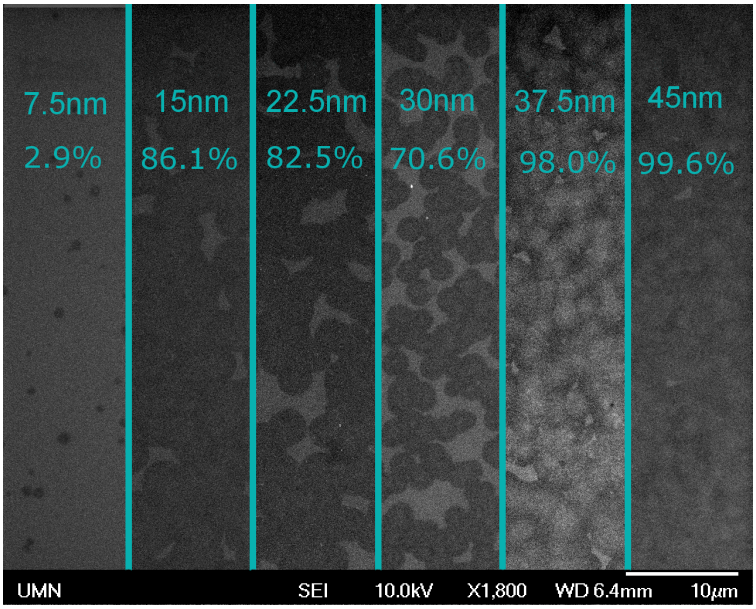

Figure 3.9: Combined SEM images of progressive thickness of YIG thin films[3].

ditions, samples were deposited for increments of 5 minutes, ranging up to 30 minutes. The deposition rate was found to be about 1.5nm per minute, leading to films ranging from 7.5nm to 45nm as measured by profilometry. These films were annealed per the conditions from section 3.5 at 825°C for 2 minutes in oxygen. As before, the films formed into a series of spots, but there was a remarkable surprise that was observed in the YIG films. There was very clear correlation between the thickness of the films and their level of crystallization, with the thinnest films being virtually un-crystallized and the thickest films being completely crystallized. Figure 3.9 shows a composite image of each of the different thicknesses of YIG after annealing. In each of the images in this figure, there is a very large increase in the crystallization of films with even an increase from 7.5nm to 15 nm. The films then remain in this state until they reach 37.5nm, where the films crystallize even more, becoming fully crystallized at 45nm. This demonstrated that it was possible to achieve full crystallization if the film thickness was large enough.

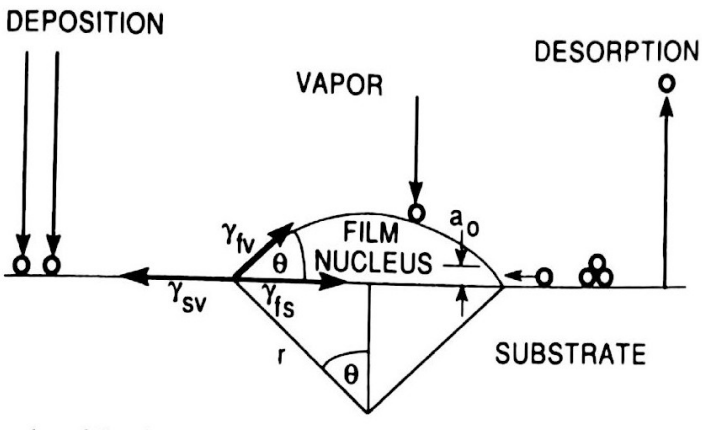

Figure 3.10: Diagram of surface kinetics in thin film nucleation[1].

3.8 Theory Behind thin Film Crystallization

Film nucleation is caused by the increase in free energy ΔG to drive the reaction into crystallization, which is affected by volume free energy ΔG_V and strain-induced energy ΔG_S. By elasticity theory the strain energy in a material G_S is giving by:

$$G_S = \frac{1}{2} Y \varepsilon^2 \tag{3.4}$$

where Y is the elastic modulus and ε is the strain. This strain is caused by misfit between the film lattice and the substrate lattice, defined by $F = (a_{sub} - a_{film})/a_{film}$. At a point very close to the film, $G_s = \frac{1}{2} YF$ because of the high interfacial mismatch between silicon and YIG. In a thicker film, this surface energy is reduced to $G_s = \frac{1}{2} Y\varepsilon$ because of the reduced surface interaction. This means that ΔG_S is lower at the surface of a thicker film than it is in an ultra-thin film because the surface is farther from the film-substrate interface[1].

At the point of thermodynamic equilibrium and consequent film nucleation, there is a critical formation energy ΔG^* defined by:

$$\Delta G^* = \frac{4(a_1\gamma_{fv} + a_2\gamma_{fs} - a_2\gamma_{sv})^3}{27a_3^2(\Delta G_V + \Delta G_S)^2} \propto \Delta(G_V + \Delta G_S)^{-2} \tag{3.5}$$

The terms γ_{fv}, γ_{fs}, and $\gamma_{sv}$are energy terms associated with surface tensions of film

formation. The terms a_1, a_2, and $a_3$are defined by:

$$a_1 = 2\pi(1-\cos\theta) \tag{3.6}$$

$$a_2 = \pi\sin^2\theta \tag{3.7}$$

$$a_3 = \frac{\pi}{3}(2-3\cos\theta+\cos^3\theta) \tag{3.8}$$

where $\theta$is the contact angle between the nucleated grains and the substrate surface. All values are shown in the diagram of figure 3.10.

The relation between the number of nucleated sites and the number of possible nucleation sites is:

$$N^* = n_s e^{-\Delta G*/k_B T} \tag{3.9}$$

The reduction in ΔG_S at the surface of the film reduces the ΔG^* nucleation energy, allowing the film the crystallize[1]. From equation 3.9 the equation for nucleation energy is $\Delta G^* = -k_B T \ln(\frac{N^*}{n_s})$. A plot of ΔG^* vs thickness is shown in figure 3.11 using values for N^* obtained from figure3.9, revealing a rapid reduction in nucleation energy as a function of thickness.

3.9 Use of YIG films as Seed Layers

With these multiple different thicknesses of YIG, the next questions is whether these films would be effective as seed layers for substituted YIG films. In fact these films were very effective as seed layers for growth of Ce:YIG and Bi:YIG. To replicate the work of [22], films of Ce:YIG and Bi:YIG were grown on the 22.5nm samples from section 3.7 using co-sputtering of Fe, Y, and the substituent, either Ce or Bi. Results are consistent with those

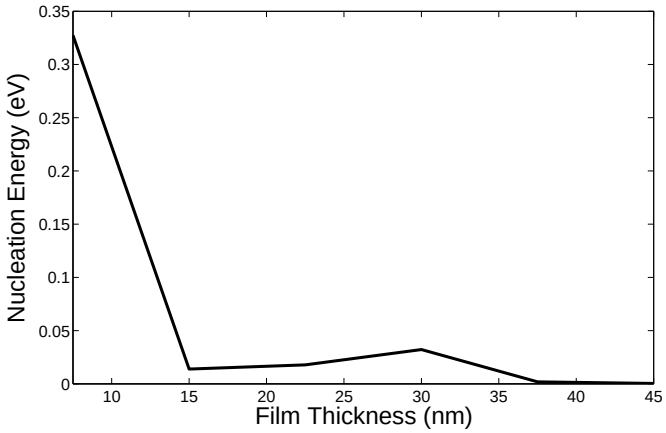

Figure 3.11: Nucleation energy as a function of film thickness

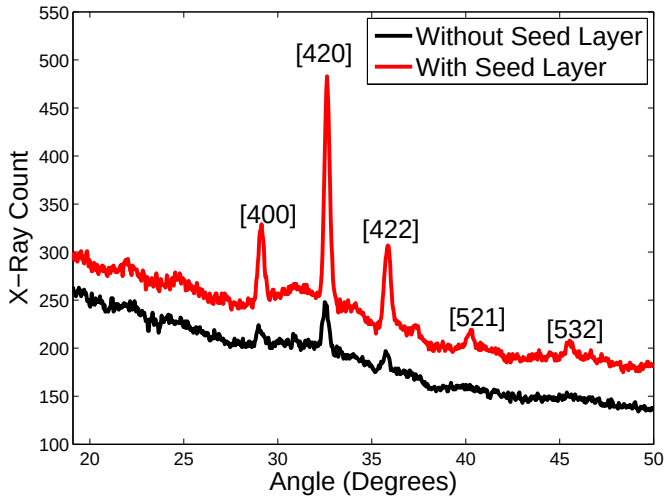

Figure 3.12: Cerium YIG grown with and without YIG seed layer[3].

of [22]. Results for Ce:YIG are shown in figure 3.12 which shows how Ce:YIG grows with and without a seed layer. It is clear from these results that garnet grows much more readily on a seed layer, as the garnet peaks of Ce:YIG become much more defined than when grown without one. The results for Bi:YIG, shown in figure 3.13, are even more striking. When grown without a seed layer, there may be formation of the YIG phase, but it is clear that other phases are present as well. By contrast, when grown on a YIG seed layer, there is formation of the garnet phase and no other phases.

Further testing emphasizes the significance of crystallization of the seed layer in the formation of the garnet phase in the substituted layer. Each of the different YIG films of

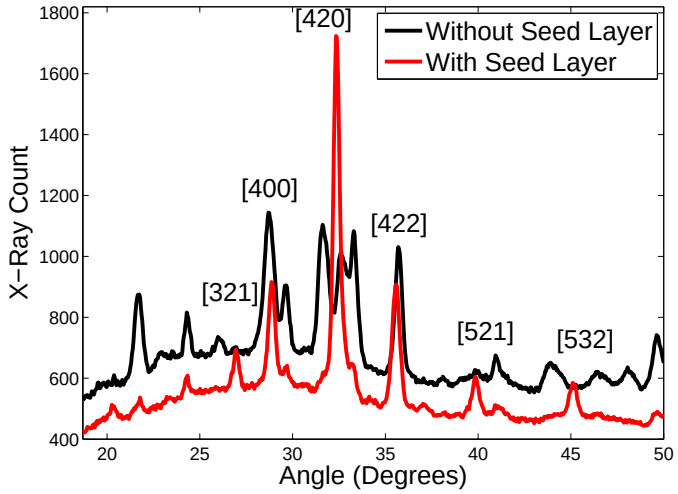

Figure 3.13: Bismuth YIG grown with and without YIG seed layer[3].

section 3.7 were used as seed layers for the growth of Ce:YIG. The XRD results shown in figure 3.14 reveal a clear correlation between YIG seed layer thickness and Ce:YIG thickness. For the thinnest seed layer, the second layer would not form into Ce:YIG at all. As the seed layer becomes thicker, Ce:YIG layer progressively becomes more defined, becoming fully crystallized when the seed layer is fully crystallized.

Ce:YIG is highly susceptible to thermal effects from annealing. At 750^{o}C, shown in figure 3.15a, the film remains free of cracks, and still forms into the Ce:YIG phase. When annealed at temperatures above 800^{o}C, the film has severe cracks in it, as shown in figure 3.15b. This film is not suitable for use in optics, so the anneal temperature for Ce:YIG must have a limit of 750^{o}C.

3.10 Magnetic Measurement with VSM

To characterize the magnetic properties of YIG, vibrating sample magnetometry (VSM) was used. In VSM, the sample is placed inside of a strong magnetic field then it is vibrated. The motion of the sample will cause a change in the magnetic flux, and because this motion is oscillating and the applied field is not, it is trivial to separate the sample-induced flux

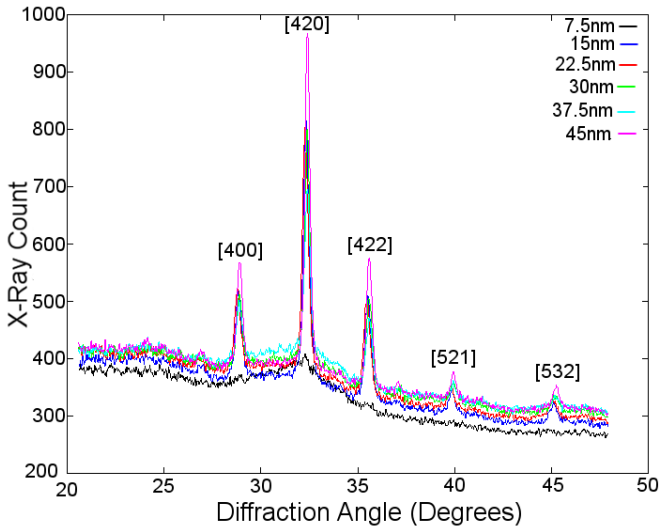

Figure 3.14: Cerium YIG grown on YIG seed layers of varying thickness[3].

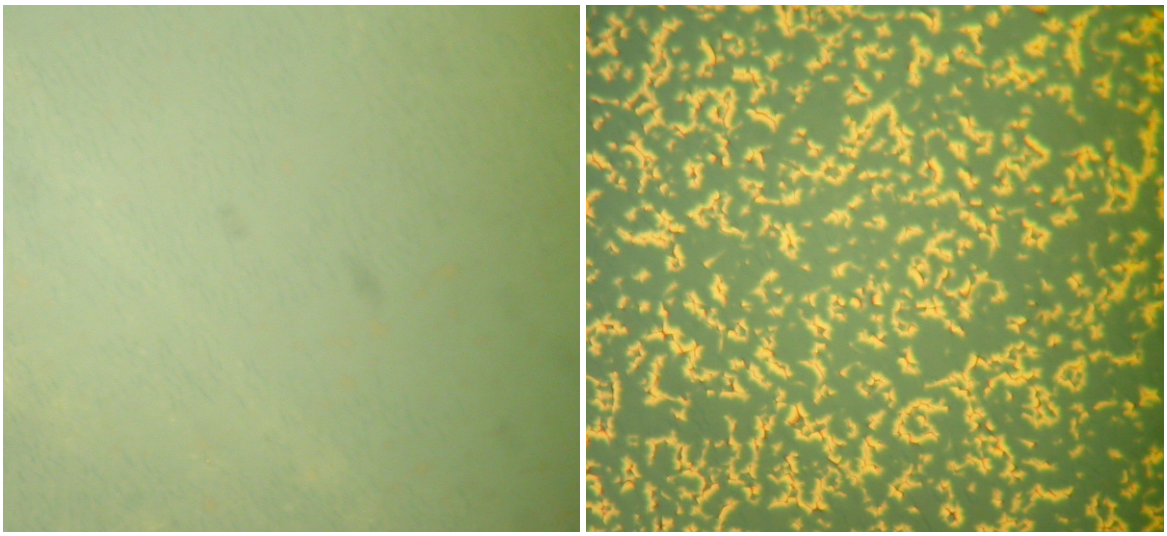

(a) 750°C (b) 800°C

Figure 3.15: Cerium YIG annealed at different temperatures[3].

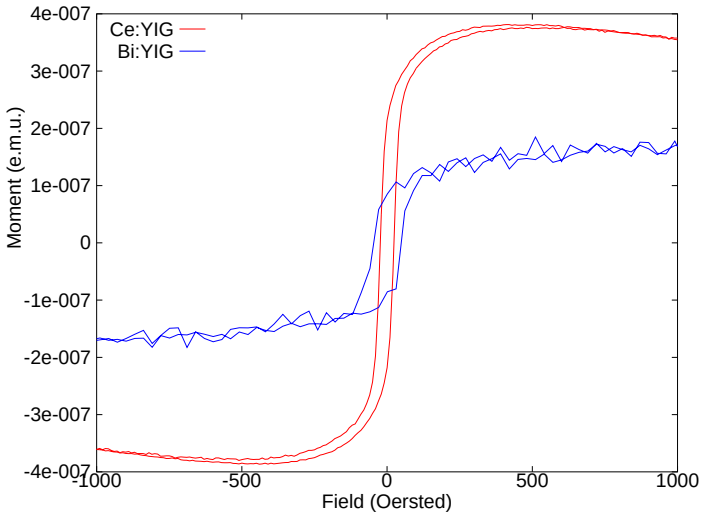

Figure 3.16: VSM hysteresis loops for Bi:YIG and Ce:YIG

from the flux of the instrument. This allows for the measurement of magnetic hysteresis in a material. The VSM hysteresis in plane measurements for Bi:YIG and CE:YIG films are shown in figure 3.16. These show that the two films due possess ferrimagnetic hysteresis, with Bi:YIG having a coercivity of 60Oe and Ce:YIG having a coercivity of 40Oe.

3.11 Magneto-optical Measurements

Measurements of the magneto-optical effect were performed on an optics bench using the arrangement shown in figure 3.17. Light is emitted from a laser source, then passed through a polarizer. The light then passes through a half-wave retardation plate. This plate is used to manually rotate the polarization of the light. The polarization of the light will be rotated twice the amount that the plate is physically rotated relative to the input polarization. For example, if the light is vertically polarized, and the half-wave plate is 4^o off of vertical, the light will be rotated by 8^o. The precision of the half wave plate is to within $.002^o$. The light then passes through the sample which is placed inside of a Helmholtz magnet. This aligns the magnetization of the sample with the direction of the propagation of the laser. The laser the hits a polarizing beam splitter (PBS) The PBS is a cube made out of two prisms with

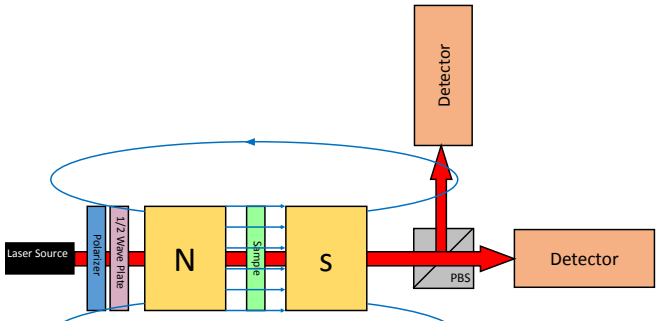

Figure 3.17: Diagram of Apparatus to measure Magneto-optical Effect

different indices of refraction. This separates the light into its transverse electric (TE) and transverse magnetic (TM) components. The amount of TE vs. TM is directly related to the polarization of the light, so there are two detectors to detect the TE and TM components. Subtracting one detector from the other gives the polarization angle of the light.

It is important to note that this system is not designed to measure *absolute* polarization of the light, but instead to measure *relative* polarization. As the half-wave plate is rotated around a complete circle, the difference in detected light between TE and TM will be a sinusoid as the amount of light oscillates between all TE and TM. When the polarization of the light is equal parts TE and TM, the difference in the detectors will be zero, between and upward and downward peak in the sinusoid. At zero, the sinusoid approximates a linear function, so any small rotations in the polarization of the light will have a linear response in the difference between the two photodetectors is zero. Therefore, in order to measure the magneto-optical rotation, the half-wave plate is rotated until the difference in the detectors is zero, then the sample is magnetized inducing a polarization rotation to move. The difference between the two photodetectors is not measured as an exact polarization, but as a difference in voltages. Because of this, it is necessary, after bringing the signal to zero, to rotate the half-wave plate by a small amount (less that $.05^{o}$) and measure the change in voltage. This voltage change is then used as a calibration coefficient for all subsequent measurements when the sample is magnetized.

3.12 Lock-in-Amplification

Optical signals can be effectively measured using a device called a *lock-in amplifier*. A lock in amplifier detects a signal of a specific frequency, then amplifies that signal, filtering out any noise that is not part of the desired signal. For the system in section 3.11, lock-in amplification is used to amplify the laser signal in the photodetectors and filter out other present light sources such as room lighting. The laser is pulsed using a frequency chopper, which modulates the optical signal at a specific frequency, and the lock-in amplifier is programmed to detect that frequency. The lock-in then detects the laser signal and filters out all signals not matching the frequency of the laser pulses. An ideal frequency for the lock-in is 282hz because 281 and 283 are both prime numbers, meaning that there will be little chance of detecting any other signals.

3.12.1 NI-Lock-in Amplifier

In order to get more accurate results for the optical measurement system, it was necessary to record and store the data from the photodetectors on a computer. This was facilitated by the use of a National Instruments CompactDAQ 9178, shown in figure 3.18. This instrument was then equipped with CompactDAQ 9215 input and 9263 output modules. These devices are generic 10khz voltage devices that are monitored using National Instruments Labview. To measure the inputs, a software-based lock-in amplifier was designed using Labview. An image of the design is shown in figure 3.19. This program takes in signals from the photodetectors and the frequency chopper and uses an NI-proprietary algorithm to produce lock-in amplification.

Because the lock-in is software-based, it's completely customizable and versatile, so several features were added into the program in addition to lock-in amplification. This program is used to control the supply current to the Helmholtz coil as well as the rotation of the half-wave plate, and a hall-effect sensor was embedded into the system to measure

Figure 3.18: NI CompactDAQ Module

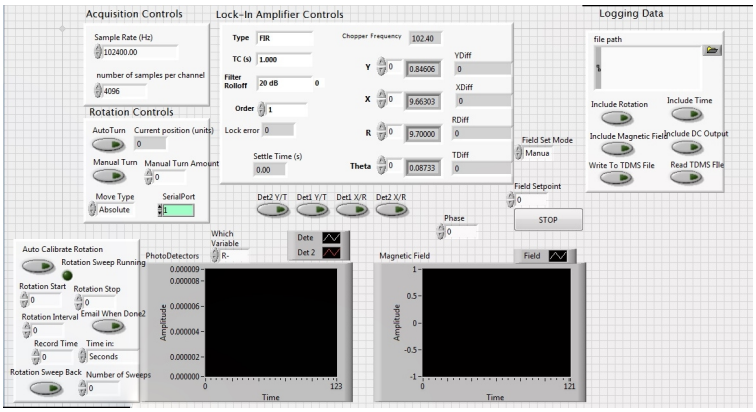

Figure 3.19: Labview Lock-in Amplifier screen

the strength of the magnetic field. Additionally, the software could be set up to perform automated measurements, and even e-mail the user when automatic measurements were complete. This was a great benefit to the magneto-optical measurement system, allowing for increased accuracy and automation.

3.13 Magneto-optical Results

For 1550nm light, measurements of Bi:YIG had a Faraday rotation of 1700^{o}/cm when saturated, and Ce:YIG films had a rotation of 3700^{o}/cm. This is currently the highest recorded magneto-optical effect in a thin film[3].

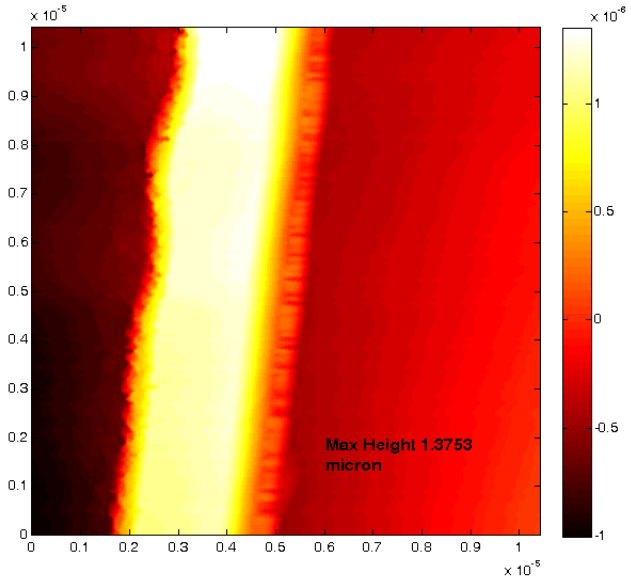

Figure 3.20: AFM image of YIG waveguide

3.14 Waveguides and AFM Measurements

In addition to making advances in thin films, part of this research was focused on advances in YIG waveguides. An important part of waveguide characterization is to understand how waveguide shape affects the transmission of light in YIG waveguides. While most waveguides are idealized as having a rectangular cross section, the actual waveguides of [26] have a trapezoidal profile, being slightly more narrow at the top of the waveguide than at the bottom. To establish an experimental profile of YIG waveguides, the waveguides from [26] were characterized by AFM, and the waveguide profile is shown in figure 3.20.

The AFM data from figure 3.20 was then imported into Lumerical FDTD, as shown in figure 3.21. The waveguide was simulated on top of 1μm of silicon oxide on a silicon substrate. Figure 3.22 shows the results of a simulation of passing 1550nm light through the waveguide, resulting in a well confined guided mode. Measurements of optical losses in these waveguides were as small as 0.1db/mm in waveguides of 1.5μm wide, confirming high transmission.

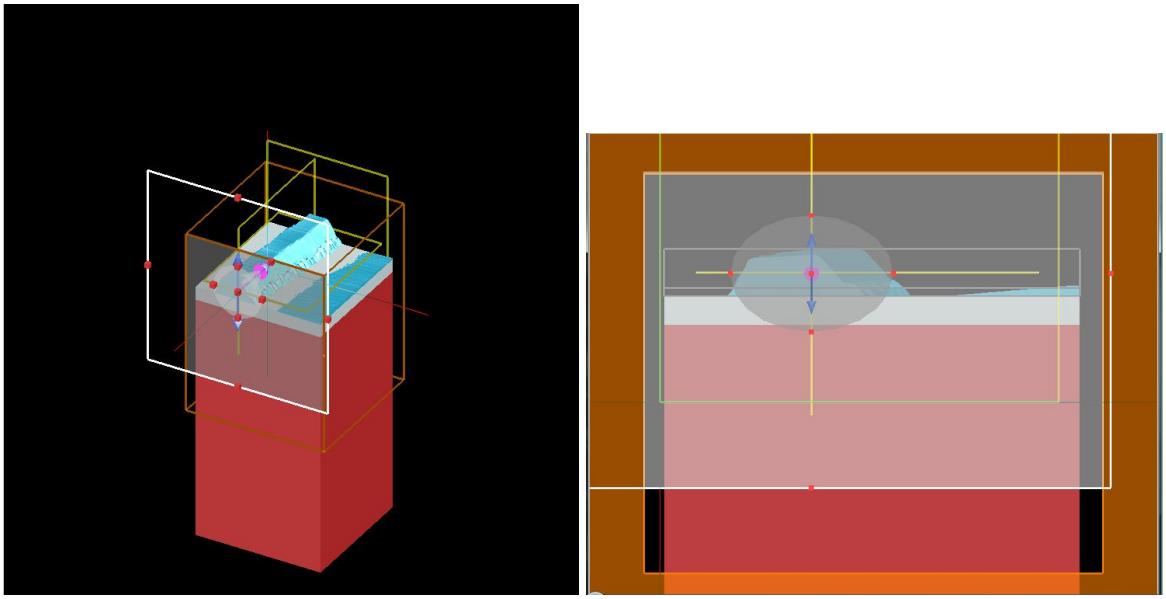

(a) Perspective View (b) Cross Section of Waveguide

Figure 3.21: AFM profile of YIG waveguides as imported into Lumerical FDTD

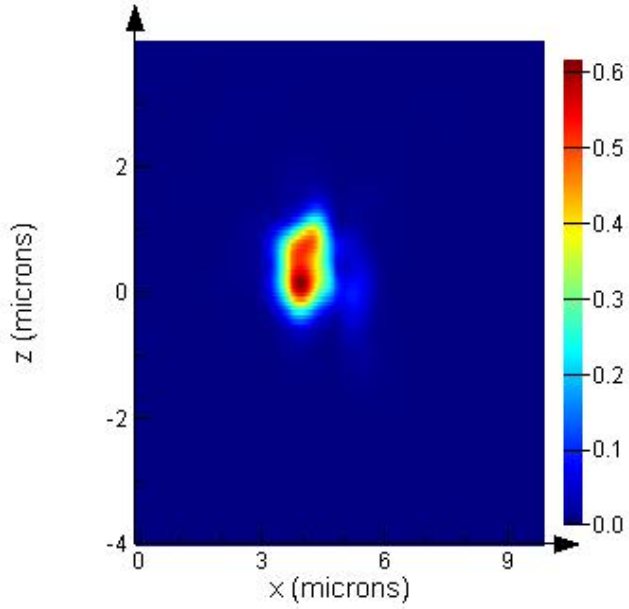

Figure 3.22: Electric field intensity of guided mode in YIG waveguide

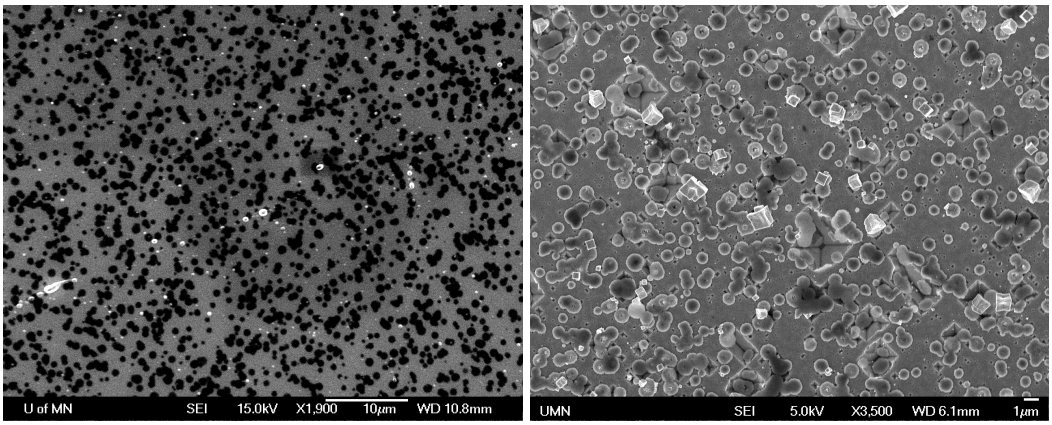

(a) Before Etch (b) After Etch

Figure 3.23: Partially Crystallized film of YIG with KOH Etch

3.15 Chemical Properties and use of YIG as an Etch Mask

YIG is a highly chemically resistant material, so it was investigated whether it would be a suitable etch mask for KOH silicon etching. This would facilitate the fabrication of YIG suspended membranes, improving magneto-optical measurement, or it could be used for MEMS fabrication. Films of partially crystallized and fully crystallized YIG, shown in figures 3.23a and 3.24a, were etched in a 50% KOH solution. The results indicate that YIG has the potential to suffice as a KOH etch mask. Figure 3.23b shows the partially crystallized sample after the etch, in which the amorphous matrix material has been destroyed, but the YIG crystallites remain. In the regions where the amorphous material has been removed, the characteristic Si {111} etch profile is visible, forming square-pyramidal indentations into the substrate surface. By contrast, the fully crystallized sample has protected the surface of the substrate. Figure 3.24b shows no such indentations, indicating that YIG survived the KOH. This demonstrates the viability of YIG as an etch mask.

3.16 Future Work

Within the last three years, a new garnet was discovered that exhibits the Faraday effect with an interesting and exploitable variation. Terbium iron garnet (TIG, $Tb_3Fe_5O_{12}$) has

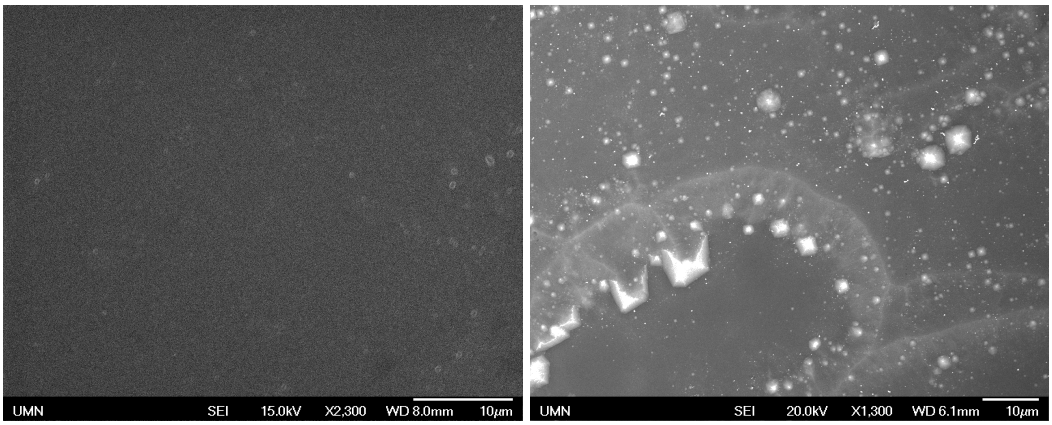

(a) Before Etch (b) After Etch

Figure 3.24: Fully Crystallized film of YIG with KOH Etch

a rotation of 500^{o}/cm in the opposite direction of YIG, and addition of Bi into the lattice of TIG results in even higher rotations. Also, unlike Bi:YIG or Ce:YIG, Bi:TIG can be grown without a seed layer, resulting in greater coupling efficiency to a silicon waveguide and more magneto-optical effect on the guided mode. One of the most likely ideas being proposed for fabrication TIG into an isolating device is to integrate it together with YIG for quasi-phase matching (QPM) applications. QPM is the process of creating a periodic structure in a mode converting waveguide to compensate for chromatic dispersion in the guiding material. It has been performed by making a waveguide of periodic segments of YIG and SiO_2[28]. While it is effective to oscillate between a magneto-optic and non-magneto-optic material for QPM, an even greater effect could be realized my oscillating between two materials with opposite rotations. It is very exciting to see the possibilities that unfold from magneto-optical materials and the the new technologies they bring about.

In addition to work with a new garnet, other research is being conducted to validate the results of section 3.8. Transmission electron microscopy has confirmed that YIG grains do not nucleate from the surface of the wafer, but begin at the surface of the film and grow downward. Because of this , it is possible to deposit a substituted layer, then the seed layer on top of it, allowing the substituted layer to be directly in contact with the surface of an SOI waveguide[29]. Additionally, it may not be the case that the surrounding material is

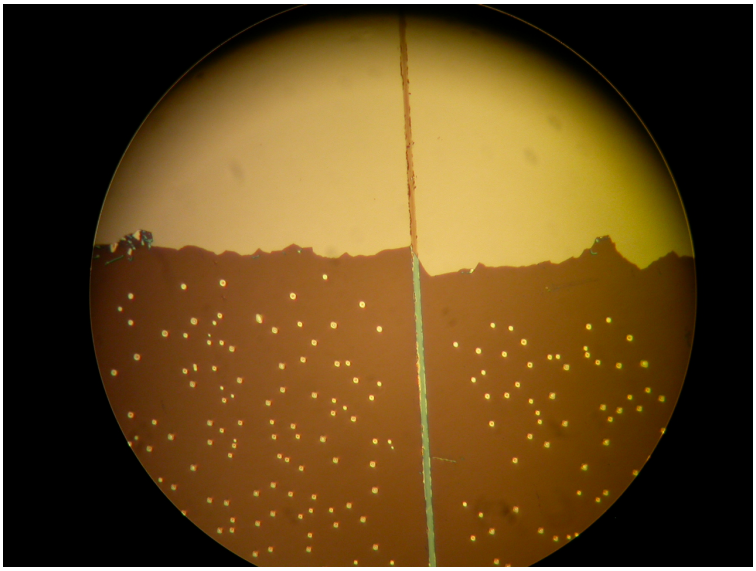

Figure 3.25: Ce:YIG grown using a YIG waveguide as a seed layer.

amorphous, but is in fact a composite of multiple phases of crystalline nanoparticles. This research is illuminating much information on YIG growth and nucleation.

Another idea being presented for a future progress is to combine the ultra-thin seed layer work with the work on YIG waveguides. Thin films of YIG can be deposited, patterned, and annealed. After this, a layer of Ce:YIG would be deposited over the entire sample. In the regions were the YIG is present, the CE:YIG would selectively crystallize, and outside of this region, it would form into cerium oxide. This has been experimented, and the results are shown in figure 3.25. The upper part of the picture shows a YIG waveguide, and the bottom half of the photograph has additionally been coated in Ce:YIG. In the region were the YIG waveguide is present, the Ce:YIG has also crystallized. In the surrounding material, the Ce:YIG has formed into another material with bubbles present in it.

3.17 Conclusion

Prior to this work, the state of the art in YIG deposition on semiconductors was the deposition of thin films of YIG for use as seed layers. This work took the seed layer concept and improved it for greater magneto-optical effect. In attempting to do this, it was discovered

that in fact the seed layers do not fully crystallize if they are too thin. From this information, a working theory was developed which explains the root-cause of heterogeneous grain nucleation using first principles. A minimum thickness was established to get full crystallization, and these fully crystallized films were used as effective seed layers for Bi:YIG and Ce:YIG. The films were then measured using a custom-built magneto-optical measuring system using Labview for data recording, and the substituted YIG films were found to have record Faraday rotations. In addition, YIG waveguides were analyzed by AFM, and the AFM data was used to perform optical simulations of transmission in YIG. These simulations show very high transparency and mode confinement. This work demonstrates significant advances in the development of YIG devices on semiconductors.

Chapter 4

Barium Strontium Titanate Films for Electro-Optical Applications

4.1 Optical Modulation

An important part of photonic systems is the ability to modulate a signal inside the optical medium. Optical modulation consists of making a signal out of light either by changing the amplitude or phase of the light as it is traversing an optical path. A commercial phase modulator is shown in figure 4.1. Like the isolator of figure 3.4, this is a bulk device, and in order to achieve monolithic integration, this device will need to be miniaturized to the micro scale. This has presented a materials science challenge similar to that of YIG but with several distinctions that make its fabrication a unique experience.This chapter will discuss the creation of a new modulating material, beginning with a discussion on the fundamentals of perovskite oxides and the effects they exhibit, and how those effects function in photonics systems. The next part of the chapter will focus on fabrication of these oxides and how to integrate them with semiconductor and dielectric platforms. The chapter will close with a discussion on waveguide development and the progress towards the fabrication of an optical modulator.

Figure 4.1: Electro-optical Modulator from Newport Optics[4]

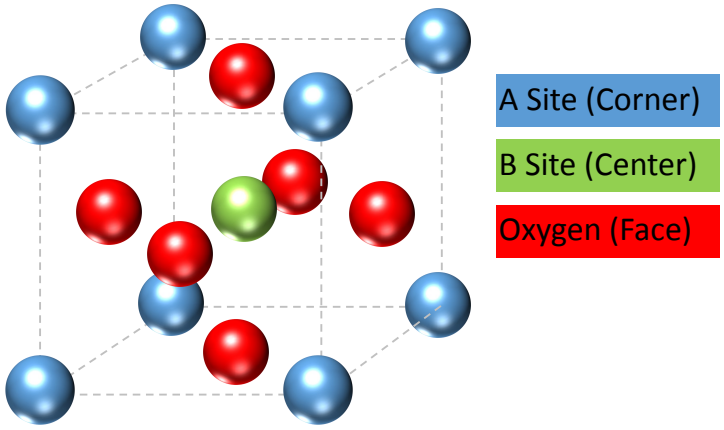

Figure 4.2: Diagram of perovskite structure

4.2 Perovskites

The perovskite structure is shown in figure 4.2. It takes the form ABO_3 , where the A atoms are cations (typically 2+) on the corners, and the B cation (typically 4+) is located in the center of the lattice. Each of the oxygen anions are located in the faces of the lattice. In the cubic phase it has the space group $Pm\bar{3}m$ and in the tetragonal phase $P4mm$. Many different atoms can occupy the the perovskite structure, consequently there are several different variations of it including $PbTiO_3$, $LiNbO_3$, and $BiFeO_3$.

Most perovskites exhibit ferroelectricity, in which there is a hysteresis in the dielectric polarizability of the material. When a sufficient charge is applied there is a physical shift of the central B cation within the unit cell, changing the symmetry of the perovskite lat-

tice from the cubic phase to tetragonal. The materials properties accordingly modify their symmetry leading to exploitable effects.

4.2.1 The Electro-optical Effect

The refractive index of a perovskite follows its symmetry. In the case of a cubic perovskite, the index will take the form of equation 4.1, having an equal index along the x, y and z directions[19].

$$\overleftrightarrow{D} = \begin{bmatrix} \varepsilon & 0 & 0 \\ 0 & \varepsilon & 0 \\ 0 & 0 & \varepsilon \end{bmatrix} \tag{4.1}$$

In a material that is uniaxial, such as a tetragonal crystal, the index of the material will be different along one of the axes due to symmetry, taking the form of equation 4.2. The two optical axes are called the ordinary axis, ε_o, and the extraordinary axis, ε_e.

$$\overleftrightarrow{D} = \begin{bmatrix} \varepsilon_o & 0 & 0 \\ 0 & \varepsilon_o & 0 \\ 0 & 0 & \varepsilon_e \end{bmatrix} \tag{4.2}$$

When an electric field is applied to a perovskite, because of the shift in the central cation, its change in symmetry results in a commensurate perturbation in the refractive index, becoming that of equation 4.2. This means that the extraordinary axis changes which direction it is pointed. Light traveling down this axis will then experience a different refractive index than if the charge were not applied. This is referred to as the *electro-optical (EO) effect* or *Pockels effec*t. This effect can be used to create an optical modulator. Light is propagated through a waveguide made of electro-optical material and can be modulated by applying an electrical signal to the waveguide to induce a phase change in the light. The EO effect is defined by equation 4.3 the formula where ϑ is the EO coefficient and E is the

applied electric field. It is quantified in units of length/volt, usually having a value on the order of 10^{-12}m/V[19].

$$n(E) \approx n - \frac{1}{2}\vartheta n^3 E \tag{4.3}$$

4.3 Monolithic Integration and Scaling

Scaling an optical modulator to fit a monolithic platform is a materials challenge unto itself, and in fact with current materials it is not possible. Unlike YIG, in which substitution into the lattice can enhance the properties enough to make integration viable, modern EO modulating materials are completely insufficient for this task. The current material used in commercial modulators like those of figure 4.1 is $LiNbO_3$, a perovskite with an electro-optical coefficient of 32.6pm/V. For quantification purposes, if a 1MV/m field were applied to $LiNbO_3$, its refractive index would change from 2.3 to 2.2998, or a .0086% difference. Analogous to YIG, this is not sufficient for monolithic integration because it requires a very long path length to change the phase of the light. This is the reason that modern optical modulators are made as bulk devices rather than on a chip. In order to reduce the path length and facilitate monolithic integration or at least a smaller device footprint, a material with a higher EO coefficient would be necessary. Some research has gone into the use of lead-titanates such as $Pb(Zr_xTi_{1-x})O_3$, but this material presents several problems. First and most importantly, lead is toxic and environmentally damaging, and is consequently not a material that industry would want to use on a wide scale. Secondly, materials with lead do not perform well in environments where ionizing radiation is present. Radiation causes a distortion of their ferroelectric hysteresis, making them unsuitable for electro-optical modulation in environments where large levels of radiation are present, such as particle colliders or space[30]. Unfortunately, these are exactly the places where optical circuits would provide the greatest benefit due to the high levels of data throughput in such environments.

Environments such as CERN, where massive amounts of data are being gathered under conditions of extreme radiation, necessitate the fabrication of optical devices that are small enough that many of them can be fit into a small area. Such devices will require a new material with a high EO coefficient and the ability to function under radiation.

4.4 Barium Strontium Titanate

Barium Strontium Titanate ($Ba_xSr_{1-x}TiO_3$, BSTO) is a perovskite with an EO coefficient of up to 1640pm/V and contains no lead. This makes it a promising candidate for EO devices. Barium titanate by itself is an electro-optical material, and the addition of strontium improves the response rate of the material, allowing it to be operated at rf frequencies[31]. As was later discovered, the addition of Sr also allows for the tuning of lattice constant, which created an additional benefit for EO modulation which will be discussed in section 4.7.

4.5 Deposition of BSTO by sputtering

Much like YIG, BSTO is a difficult material to deposit onto semiconductor platforms due to extreme differences between their thermal expansion coefficients. Barium titanate has a thermal expansion even larger than that of YIG, $15.7*10^{-6}/^oK$, over seven times that of silicon. Furthermore, the lattice of BTO is not cubic, but tetragonal. Pure strontium titanate, however, is cubic with a lattice parameter within 1% of that of silicon. Frequently STO is grown epitaxially onto a silicon substrate, then the BTO or BSTO epitaxially matches to it along the a-axis, with the b-axis being normal to the plane of the film. This is usually performed at very high temperatures using composite targets made of a predetermined composition of BSTO. This results in very slow deposition rates of 5Å/min which are useful for making thin films for capacitors, but the films necessary to make a device such as a modulator will require a film that is thick enough to guide an optical mode[32]. This is at least

500nm, so a method to reliably grow optically thick films of BSTO with high transparency and sufficient EO coefficient needed to be developed. Also, because of the mismatch in thermal expansion between BSTO and Si, methods must be developed to minimize thermal stresses which could crack the films.

Fortunately, the previous work on YIG already provides a framework for which complex oxides can be grown efficiently with no crack formation. Consider if, analogous to the fabrication of YIG, targets of Ba, Sr, and Ti were sputtered in an oxygen partial pressure then crystallized by RTA. This would provide a way to grow BSTO films quickly while minimizing thermal processing, just as was done with YIG. The rest of this chapter will focus on the fabrication of BSTO by this method, with special attention paid to deposition parameters, and the unique considerations that go with the deposition of this material.

4.6 Preliminary Investigation of BSTO Depositions

Nowhere among the literature had BSTO been made using metal targets by co-sputtering. On the one hand this was an exciting challenge, being able to invent a new process to make a material. However, there were also many risks involved, as it was unknown whether BSTO could even be made with co-sputtering. Unlike YIG, which has been thoroughly explored, making BSTO with metal targets was relatively unknown. How much would these targets oxidize? What were their deposition rates? How much power was needed for each target? These were all questions that needed to be answered. With that in mind, the first part of the process was simply to establish how each of the different targets behaved and how each of the different parameters would affect film formation.

Based simply on their position in the periodic table, it can be surmised what kind of behavior each of the elements of BSTO will have. Ba and Sr are both group II elements and are not naturally found in their elemental form. This means that these materials are highly reactive. As a result there are several considerations that must be taken when handling,

storing, and using these materials. Firstly, both of these materials are highly susceptible to oxidizing, and will in fact form a layer of rust in air in a matter of minutes. For this reason, it is essential that these materials are exposed to atmosphere for a minimum amount of time. Immediately upon removal from their packaging, they must be cleaned with isopropyl alcohol, dried, and placed into the vacuum chamber as quickly as possible, and the heavy oxidation of these metals requires a pre-sputter of approximately two hours to remove. Additionally, it is very important that these targets are never exposed to water, as it could cause them to explode.

Sputtering of Ba and Sr in an oxygen atmosphere had some surprising results. It would be expected that the more reactive of the two elements would be Ba, since that element is below Sr on the periodic table. However, it turned out that Sr is the most reactive element. After several depositions in oxygen, the Sr target will be covered in a large amount of strontium oxide dust. This yields two results. The first is that because of this particulate, Sr must be deposited using an rf plasma, and this plasma is still very unstable and difficult to maintain. When using the automatic tuning, the system will attempt to adjust but with Sr, there is no stable point, and the automatic tuning system will end up overcompensating and minimizing the load or tune parameter. Consequently it is necessary to manually adjust the load and tune parameters for the rf plasma rather then letting the system automatically do so. In order to light a plasma on the Sr gun, set the load and tune to manual, then adjust the load and tune parameters to approximately 50%. Light the plasma using a low power below 40W. Because the system is in manual, the load and tune parameters must be adjusted by hand to minimize reflected power. If the reflected power will not minimize, move the load slightly off of the minimum reflected power, then adjust the tune capacitor. It is often the case that a stable point is located off of the minimum reflected power. The second result of the dust formation on the Sr gun is that the Sr gun must be cleaned every few months using phosphoric or citric acid.

Barium, by contrast, does have nearly as much oxidation as strontium does. Conse-

Argon Flow (sccm)	Oxygen Flow (sccm)	% Sr in Film	% Ti in Film
43.3	0	56.8989071	43.1010929
43.3	1	76.47058903	23.52941097
42.4	2.1	82.61339098	17.38660902

Table 4.1: Oxygen Flow rates in STO depositions and resulting stoichiometries

quently, Ba can be deposited using a DC plasma instead of rf, and the barium target is not as susceptible to as much barium oxide dust depositing on the gun. Related to this, the deposition rate for Ba is about twice that of the rate for Sr.

Titanium also behaved in an unexpected yet beneficial way. It would seem reasonable that titanium would require the use of an rf plasma due to its strong oxygen gettering nature. It was soon discovered, however, that the oxidation layer is thin enough that the metal will still sputter with a DC plasma as long as the amount of oxygen in the chamber is kept below a certain flow rate. Initial investigations demonstrated that maintaining lit plasmas required a a chamber pressure of 35mtorr, so to test the effect of increased oxygen in the chamber, the pressure was kept at 35mtorr, and the flow of oxygen and argon were adjusted to maintain this pressure. Table 4.1 shows the EDS measurements of STO films on copper substrates using a 150W plasma on Sr and 150W on Ti in varying oxygen flow rates. Copper was used as a substrate for stoichiometric analysis because during EDS, the energy peaks of copper are very far away from those of Sr and Ti making it very easy to discern between the film and the substrate. Table 4.1 shows a clear correlation between the amount of oxygen present in the deposition and the ratio between Sr and Ti. When the oxygen flow rate was 2.1 sccm, the amount of Ti in the film was only 17%, therefore all future depositions were performed with a flow of 1.0sccm of oxygen. This allows there to be a reactive sputter without completely suppressing the deposition of titanium. More oxygen would require very high power to be applied to the Ti resulting in excessive bias voltages applied to the target.

The next step in the process was to establish if adjustments in plasma power have an effect on film stoichiometry, using two elements, Sr and Ti for simplicity. It has already been

Sr Power	Ti Power	% Sr in film	% Ti in film
150	150	76.47058903	23.52941097
120	235	34.70701734	65.29298266
150	235	53.58727734	46.41272266
150	250	46.0342153	53.9657847

Table 4.2: Plasma powers of Sr and Ti and their effect on film stoichiometry

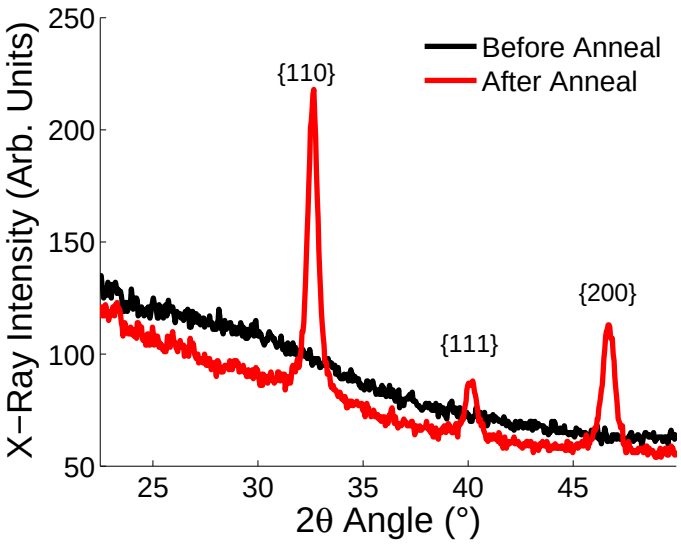

Figure 4.3: STO Films on silicon

established from section 2.2.1.2 that the relation between plasma power and composition, and depositions of STO behave according to this trend. Table 4.2 shows a clear correlation between power and the concentration of the corresponding element in the films. For further STO depositions, a powers of 150W for Ti and 235W for Sr will produce an STO film. Films were then deposited on silicon substrates using this method, followed by RTA for 2 minutes in an oxygen atmosphere at 900^{o}C. XRD patterns of these films are shown in figure 4.3 for the sample before and after annealing. Films successfully formed into the STO phase after the RTA step.

With a proven method demonstrated to make perovskite, the next step was to add the third element and fabricate BSTO. The addition of Barium into the formula created a new series of complications for the depositions. Initial literature research on phase diagrams of the Ba-Ti-O system indicated that if the correct stoichiometry of perovskite was achieved,

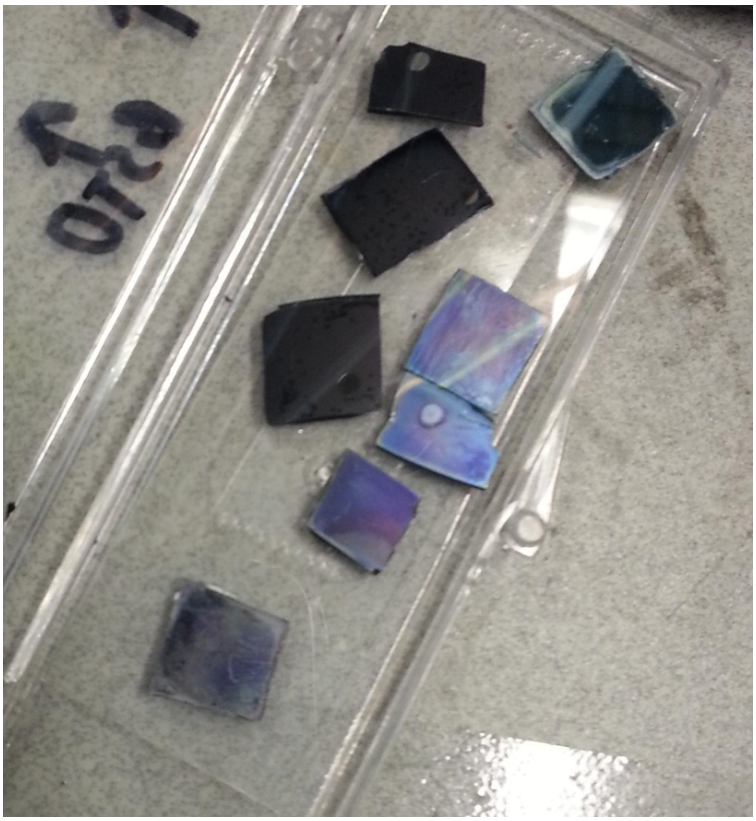

Figure 4.4: Initial attempts to make BSTO films

the BSTO phase would form just as it had with STO. Initial depositions attempting to make BSTO resulted in films that had a translucent appearance similar to that of frosted glass. Several films are shown in figure 4.4, all of which have this frosted appearance. Analysis of film morphology under scanning electron microscope in figure 4.5 shows the film to be made of many particles rather than a smooth film, which explains their appearance. XRD results for these films did not yield the correct phase, and in fact were not identifiable according to their patterns.

From the information in phase diagrams, intuition suggested that the stoichiometry of these films was not correct. Also, one of the samples, which was cleaned in water rather than in acetone, formed into the perovskite phase. Initially it was thought that the water had oxidized the film, filling in oxygen vacancies, but this turned out not to be the case. Also, backscatter SEM from figure 4.6 shows that there is a difference in the composition of the spots and the surrounding material. Backscatter SEM shows an image in which the

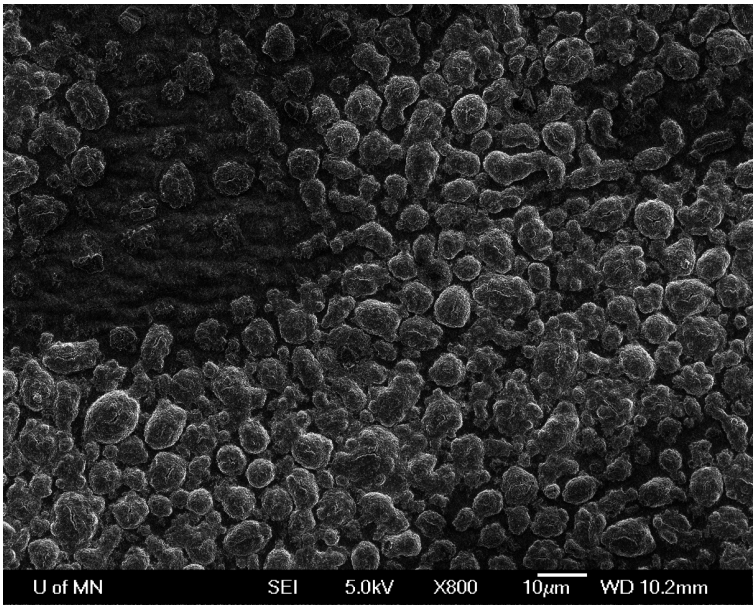

Figure 4.5: SEM image of initial BSTO films

heavier element appear brighter than lighter elements. The image of figure 4.6 shows that the particles are made up of a lighter element, while the regions that surround the spots are made up of a heavier element.

All of these results corroborate the fact that the film does not possess the stoichiometry necessary to form the BSTO phase. Confirming this hypothesis, however, requires specialized to techniques. The X-Ray emission line of Ti is 4.5keV and the emission line of Ba is 4.46keV. This is within the linewidth of EDS measurement of 150eV meaning that EDS is an insufficient to analyze the amount of Ba and Ti in these films. Instead WDS, must be used. WDS is a more accurate process, but is somewhat more complicated because it requires calibration to a standard every time the system is used.

WDS results confirmed that indeed the stoichiometry of the sample that had been cleaned in water was that of BSTO. This was not, however, due to oxidation of the sample. The real reason that the sample had the correct composition was because Ba is water soluble element, and the cleaning step had removed excess barium, resulting in the sample having the correct stoichiometry.

From these results, it was clear that in order to make BSTO, the amount of Ba would

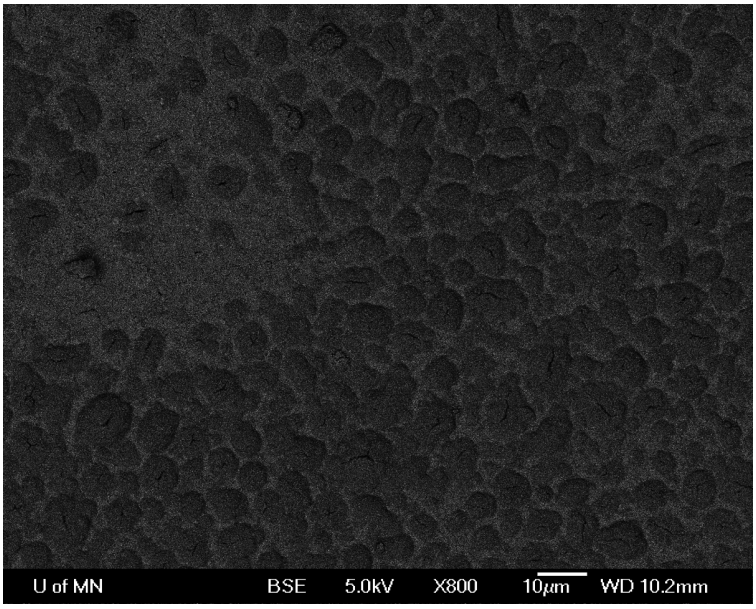

Figure 4.6: Backscatter electron image of initial BSTO films

need to be reduced. Films were then fabricated with the same gas parameters and Ti plasma power as previous depositions, but with significantly reduced power to the Ba target and increased power to the Sr Target. XRD analysis of these films is shown in figure 4.7. Interestingly, all of these films formed into the BSTO phase after RTA, indicating that like STO, BSTO crystallizes when the proper stoichiometry is achieved. Also noticeable from figure 4.7 is that as the Ba plasma is increased, the position of the maxima of the XRD pattern reduce, indicating an increase in lattice constant. This leads to a very important question:how precise is the control of the stoichiometry of the films, and is it therefore possible to engineer a film to have a specific composition?

4.7 Tunable Stoichiometry of BSTO Films

If the deposition rate of any given element can be controlled simply by an adjustment of plasma power, then achieving an engineered film of BSTO should be simply a matter of figuring out the relation between plasma power for each element, and then setting the powers to whatever is needed for any given film. There are two complications to this

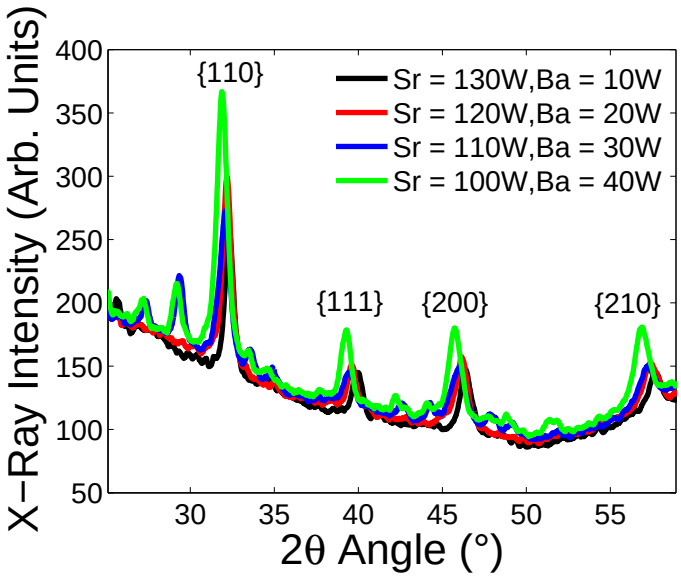

Figure 4.7: Films of BSTO with reduced Ba plasma power

procedure, however. The first is that while the plasma power does directly correlate to composition, interactions among the plasmas of adjacent guns have the potential to generate non-linearities. Secondly, stoichiometric analysis for BSTO can only be performed via WDS, which is a more time-consuming procedure to perform than the standard EDS. A novel method was needed to establish the deposition rates for Ba, Sr, and Ti using EDS. This is possible if the deposition rate for each gun is independent. When that is the case the total composition of the film is simply the combined deposition rate of each of the three constituent elements according to equation 2.1. This means that by finding the deposition rate of Ti to Sr, and Ba to Sr, the results of the two systems can be combined into a single system for BSTO.

The first material system to be examined was STO. Because Ti must remain constant in a 1:1 ratio with the combination of the other two elements in BSTO, Ti plasma power was kept at a constant power of 150W throughout all STO depositions, and all gas settings were kept at their previous values. Sr plasma power was varied from 25W to 150W, and the results are shown in figure 4.8. There is a nearly linear relation between Sr plasma power and Sr content in STO films. Varying the Sr content in BaSrO films had similar results.

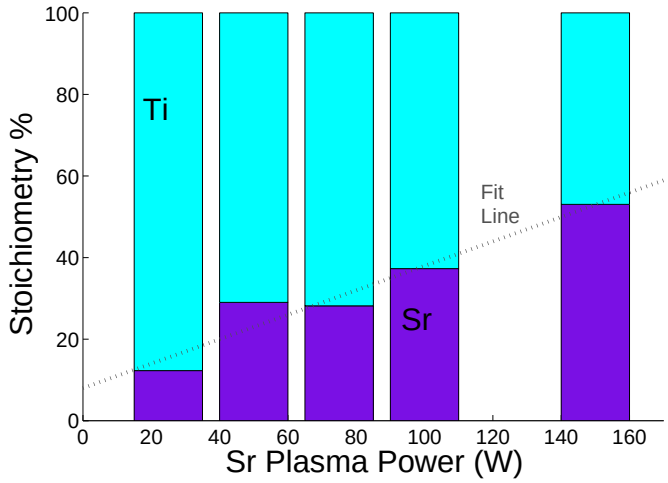

Figure 4.8: Sr in STO films as a function as a function of Plasma power in Sr

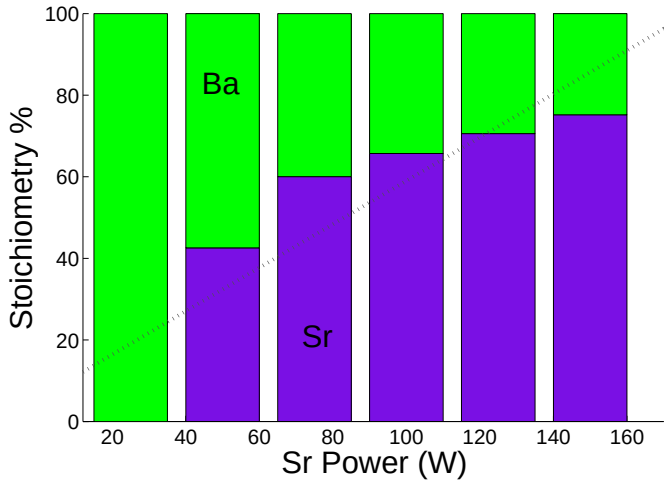

Figure 4.9: Barium strontium oxide films, varying strontium power

Films were deposited with a constant Ba power of 40W and varying Sr power. Figure 4.9 shows the results, which again show a strong linear correlation between plasma power and deposition rate for Sr. The same set of experiments was then performed for Ba. Ba plasma power was varied with a constant Sr plasma power of 150W. The results, shown in figure 4.10, show that Ba also has a linear relation between plasma power and deposition rate.

Using this information, it is possible to establish a relation that can be used to make BSTO films with engineered stoichiometries by assuming the Ti deposition result is constant and deriving from it. Consider that the amount of Ti in a film (in moles) is X_{Ti}. The

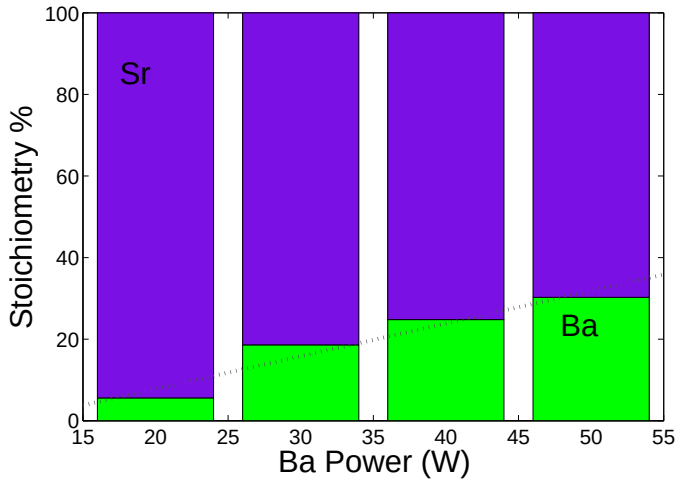

Figure 4.10: Barium strontium oxide films, varying barium power

variation in Sr content as a function of Sr plasma power P_{Sr} can only be measured as a ratio to the amount of Ti in the film. Therefore calculating the amount of Sr in the film is defined as $X_{Sr}(P_{Sr}) = (M * P_{Sr} + B) * X_{Sr}/X_{Ti}$ where M is a linear constant that maps Sr deposition rate to plasma power. The same calculation can then be recursively performed on the Ba-Sr system to establish a Ba deposition rate. The final relation found between stoichiometry and plasma power for X_{Sr} and X_{Ba} was found to be $P_{Sr} = 12941X_{Sr} + 1466$ and $P_{Ba} = 6740X_{Ba} + 1471$. Following this set of equations, samples were deposited onto silicon substrates according to table 4.3. WDS performed on this series of films revealed that they had almost exactly the stoichiometry that had been attempted for each film. The results are shown in figure 4.11, which compared the attempted composition of these films to their actual composition.

4.8 XRD Analysis and Lattice constant

The BSTO films from table 4.3 were characterized by XRD. The results are shown in figure 4.12, in which the peaks of the more Ba-rich films have shifted to the left indicating that as the amount of Ba in the films increases, the lattice constant increases linearly in perfect agreement with Vegard's law. The lattice constants of the BSTO films are shown in figure

Ba amount	Ba Plasma Power	Sr Plasma Power
0	0	144
0.1	21	131
0.2	28	118
0.3	35	105
0.4	42	92
0.5	48	79
0.6	55	66
0.7	62	53
0.8	69	40
0.9	75	28
1.0	82	0

Table 4.3: Table Of Sputter Powers

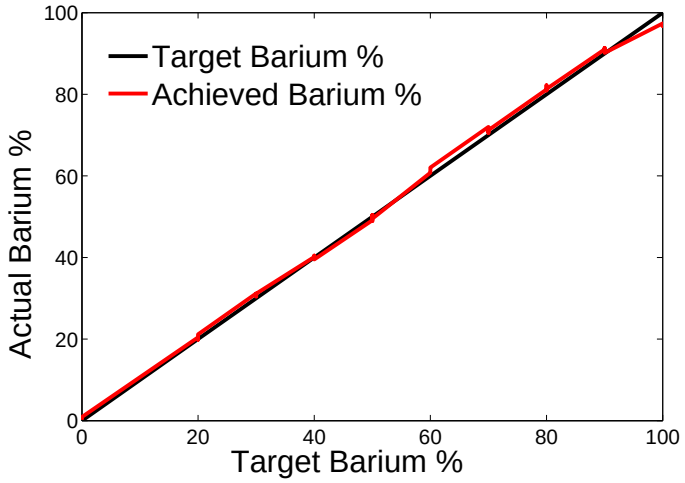

Figure 4.11: Attempted Barium percentage compared to achieved percentage in BSTO films

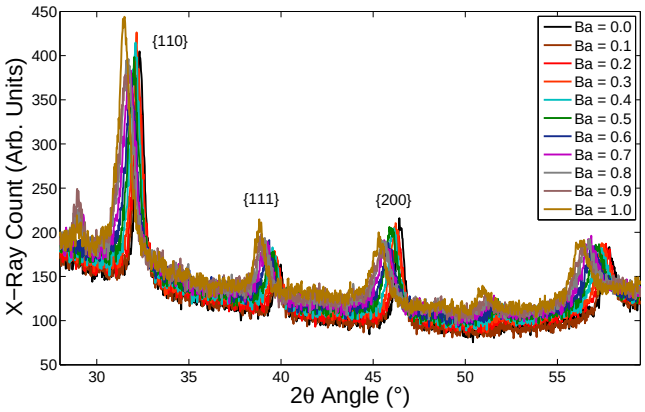

Figure 4.12: XRD results for varying compositions of BSTO

4.13, with a line comparing the values to that of bulk BSTO.

The lattice constant of pure STO is larger than that of bulk, while that of more Ba-rich samples are smaller than that of bulk BSTO. This indicates that there is film stress present in these films, and that this stress is tensile for more Sr-rich films, but compressive for more Ba-rich films. This is consistent with the films being stressed by their substrate. STO is under a tensile strain because its lattice constant is smaller than that of Si, while BTO is larger and undergoes a compressive stress. Since XRD measures the normal-to-plane spacing, it can be assumed by Poisson's mechanics that the in-plane stress of STO is compressive and and for BTO it is tensile. At a composition of approximately of $Ba_{.15}Sr_{.85}TiO_3$ there is a region of the graph that is not increasing, where the film appears to be under no stress. This is the ideal composition for using BSTO as an electro-optical modulator. If the film is under stress, it will be strained to the point that it is bound from being able to undergo a phase transition. In the absence of film-stress, the lattice is free to move in any direction, allowing it to undergo the necessary phase transition under an applied electric field.

4.9 Other BSTO Deposition Parameters

In addition to the Ba:Sr ratio, other parameters were explored to determine their effect on BSTO film formation. Others who have made BSTO films using composite BSTO targets

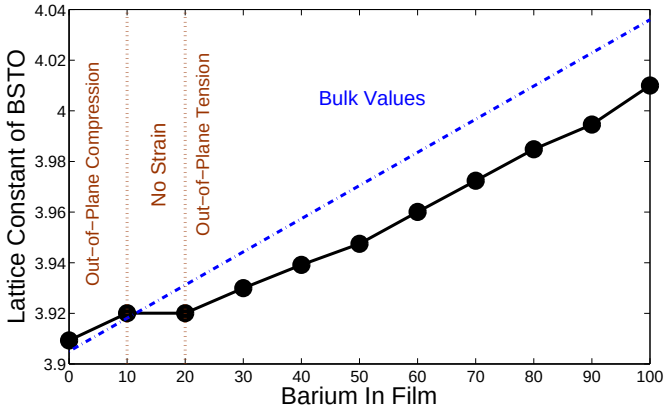

Figure 4.13: Lattice constants of BSTO films as a function of barium content

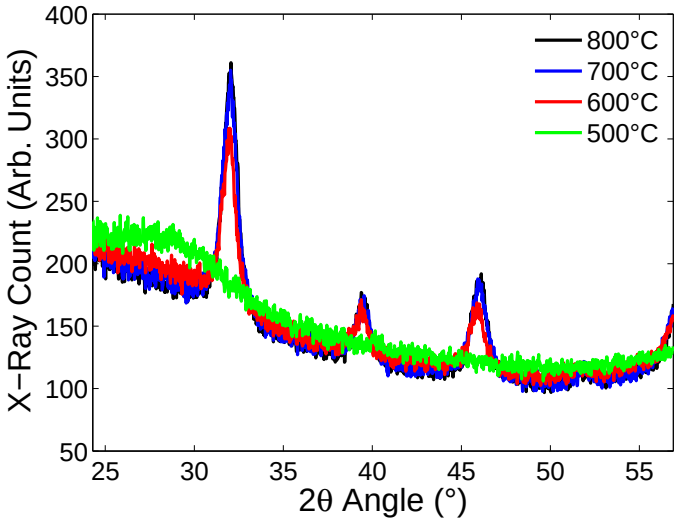

Figure 4.14: XRD patterns of BSTO films annealed at different temperatures

have been able to anneal them at lower temperatures than 900°C. In order to corroborate this, BSTO films on Si substrates were annealed at different temperatures to see if they would still form into the BSTO phase. Figure 4.14 shows the XRD patterns for each of these film. All films crystallized into the BSTO phase except those annealed at 500°C. This indicated that BSTO will form at a minimum temperature of 600°C, which confirms the results of other papers, however, the XRD peaks are more defined with an increase in temperature. For this reason, all subsequent depositions were performed at 900°C.

Different substrates were also explored to see if BSTO would grow on them as well. While BSTO films on silicon are useful for their experimental utility in determining how

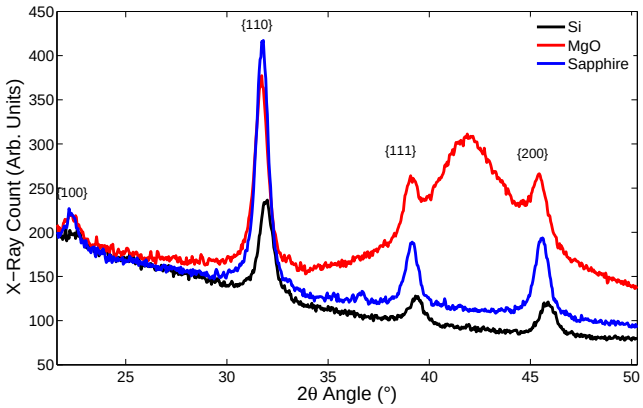

Figure 4.15: XRD patterns of BSTO films grown on different substrates

to deposit BSTO, other substrates are necessary for optical applications. Silicon has a refractive index of 3.8, while most BSTO has values in the range of 2-2.5. This means that if a waveguide of BSTO were to be fabricated on Si, the substrate would absorb all of the light away from the waveguide. In order to guide light in the film, the BSTO must deposited onto something with a lower index. Two other materials, MgO and sapphire, were investigated to see if BSTO would grow on them. From the XRD results of figure 4.15, it is clear that MgO and sapphire can be used as substrates for BSTO films. For the fabrication of BSTO devices, sapphire is a better choice because it is not a hygroscopic material.

4.10 Spectroscopic Ellipsometry

Since these films are to be used for optical applications, it is especially important to establish their optical properties. Each of the films from section 4.7 was scanned for index of refraction by spectroscopic ellipsometry. The results are shown in figure 4.16, in which the films with a higher concentration of Ba have a higher index of refraction than those that are more Sr-rich. Spectroscopic ellipsometry was also used to measure losses, which were found to be below the limit of detection, indicating highly transparent films.

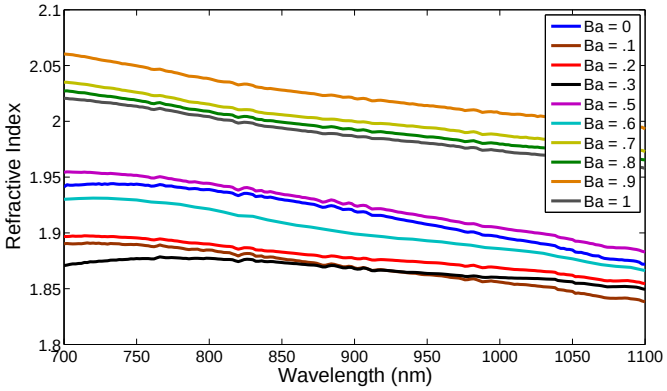

Figure 4.16: Spectroscopic ellipsometer scans of BSTO films

Figure 4.17: Capacitor design for Impedance spectroscopy measurements

4.11 Impedance Spectroscopy

To characterize the dielectric constant of BSTO films, impedance spectroscopy was used. Impedance spectroscopy the measurement of the impedance of a sample at multiple different frequencies. The capacitance of the sample is related to the impedance by the familiar formula $Z_{Cap} = 1/(\imath\omega C)$ where Z_{Cap} is the impedance of the sample. By sweeping across frequencies ω, the capacitance of the sample can be found as a function of frequency. For these experiments, samples were created according to figure 4.17. The structure consists of two electrodes on top of a BSTO film. The electrodes are 100μm wide, 100μm apart , and 7mm long. Impedance was measured across the two Al electrodes from a range of 40hz to 2Mhz. Impedance spectroscopy results are shown in figure 4.18. These results show that BSTO films (shown in the black curve) have a dielectric constant of approximately 8000.

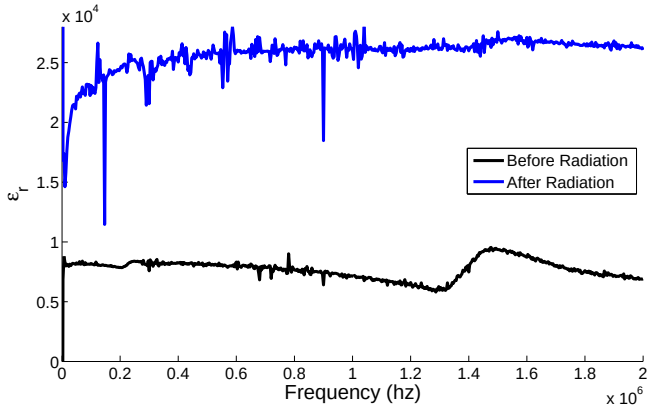

Figure 4.18: Impedance Spectroscopy of BSTO films

4.12 Measurement of Electro-Optic Effect

There are several methods to measure the EO effect, all of which are based upon the fact that when light enters into a dielectric medium, its wavelength is reduced proportionally to the index of the medium. Consider the structure in figure 4.19. This structure the *Fabry-Perot cavity* and is used to create optical resonance. It consists of two reflectors with a a dielectric material sandwiched between them. In order for the light inside the cavity to interfere constructively, the distance between the two reflectors must be an exact multiple of wavelengths apart, or more simply, $nd = N\lambda$, where n and d are the index and distance of the material, respectively. The distance from one side of the cavity to the other must be a value of N wavelengths apart[13]. When this is achieved, constructive interference occurs, and light remains inside the cavity. This is known as the *resonance condition*. If the dielectric between the two reflectors is an EO material, then when an electric field is applied to it, the index of the material will change, inducing a perturbation the resonance condition of the structure. Measuring the reflectivity or transmissivity of the structure with a spectrometer would detect this change in resonance. Fortunately, the two reflectors of the structure are metal, allowing them to be used as electrodes to supply the electric field across the cavity. Methods to attempt to fabricate this structure are shown in the next sections.

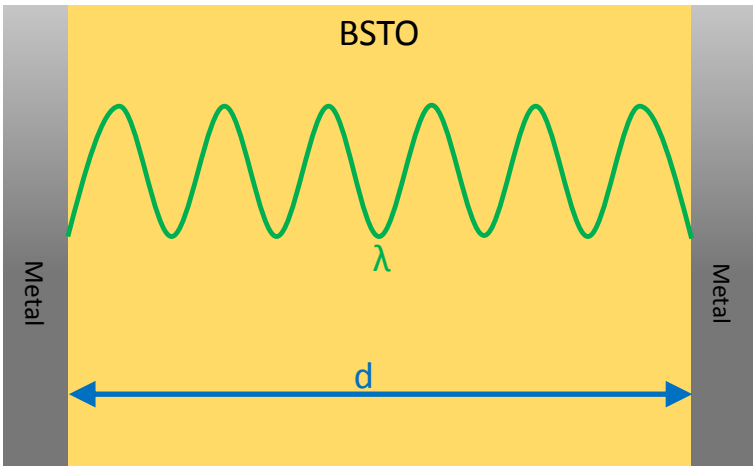

Figure 4.19: Fabry-Perot Cavity

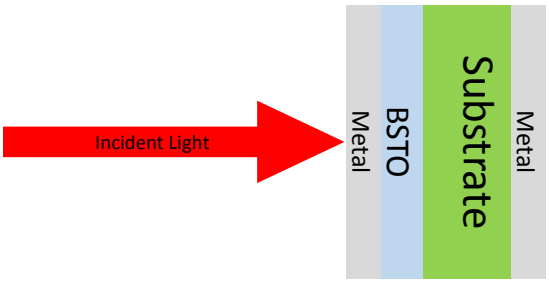

Figure 4.20: Initial Design of Fabry-Perot Structure

4.12.1 Fabry-Perot on Silicon

One of the first structures to be attempted is a basic Fabry-Perot resonator like that shown in figure 4.20. It consists of a BSTO film on double-polished silicon. After deposition of the BSTO layer, two layers of metal are deposited onto either side of the wafer. A voltage is then applied to the two electrodes to induce an EO effect in BSTO.

For this configuration, light is traveling not just through the film, but through the substrate as well. this modifies the resonance condition to $n_{film}d_{film} + n_{substrate}d_{substrate} = N\lambda$. This poses a problem because $d_{substrate} \gg d_{film}$ and $n_{film} \sim n_{substrate}$, meaning that a resonance change will not be detected because all of the resonance will be caused by the substrate rather than the film. Simulations using Lumerical FDTD confirmed this phenomenon. For this reason, the substrate had to be thinned by by an RIE process called deep reactive ion etching (DRIE). DRIE uses SF_6 gas to reactively etch through the silicon, then

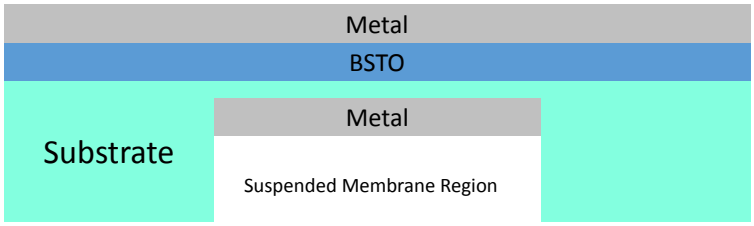

Figure 4.21: Suspended membrane design

coats the sidewalls in a polymer to protect them. This is done in cycles, etching for a few seconds and a few microns then depositing for a few seconds, taking approximately 2 hours to etch through an entire wafer. This results in very vertical sidewall etch into the wafer and very deep etching, all the way through the wafer if necessary.

In order to be able to still handle the sample, the edges of the wafer were coated in crystal bond to keep them from etching, resulting in the formation of a suspended membrane in the center of the sample. The suspended region is then coated in metal, allowing the structure to be used as a Fabry-Perot Resonator. Unfortunately, it was later discovered that this structure is unsuitable for EO applications due the extremely high dielectric constant of BSTO. When two materials are stacked on top of one another in a capacitive structure, the amount of electric field will be proportionally divided by their dielectric constant. Thusly the material with a lower dielectric constant will have more field across it, and that with the higher dielectric constant will have less proportionally. From section 4.18 it is already known that BSTO has a dielectric constant of over 8000. Silicon has a dielectric constant of 11.9, so it will end up absorbing all of the electric field in the sample, and effectively none of the field will be in the BSTO film.

4.12.2 BSTO Films on ITO/AZO

Another approach to measuring the EO effect is to build a partial Fabry-Perot structure. The structure is shown in figure 4.22 and consists of a silica substrate coated with indium tin oxide (ITO) then BSTO, then a metal reflecting layer. ITO is a transparent conductor that serves as a second electrode. Light is then put through the stack, and the index change

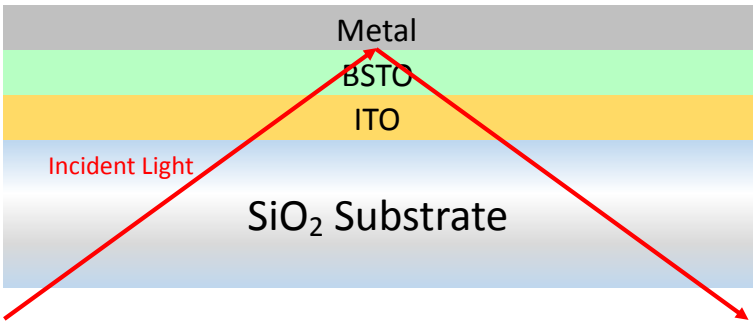

Figure 4.22: EO Measurement Structure based on ITO

in BSTO should as in section 4.12.1, induce a detectable change the resonance condition in the structure.

The first question this introduces is whether BSTO will successfully deposit onto ITO coated silica. To determine this, samples of ITO coated glass were used as substrates for BSTO deposition. The ITO coated glass was purchased from Sigma-Aldrich, and was a specific alumino-silicate designed to withstand annealing temperatures of up to 950°C. XRD patterns of the BSTO-ITO bi-layer are shown in figure 4.23 which show that the BSTO film has grown on the ITO phase. The BSTO films on ITO were then analyzed by optical reflection spectroscopy. The results are shown in figure 4.24 for cases of no applied bias, a 10V bias, and a 20V bias across the two electrodes. There is a small difference between the peaks indicating a slight EO effect. This effect, however, is very small, probably within 1nm, making spectroscopy somewhat less than adequate for measurement. Therefore a more accurate measurement method must be used.

4.12.3 Ellipsometric Measurements

A method that was found to be the most accurate was to measure the index of the BSTO using spectroscopic ellipsometry. A diagram of the process is shown in figure 4.25 in which samples of $Ba_{0.15}Sr_{0.85}TiO_3$ on Si were coated with two Al electrodes 1/4" (6.25mm) apart, similar to the structure of section 4.11 but with a larger gap for the ellipsometric scanning spot. A voltage of 100V was applied to the two electrodes. Unlike the previous struc-

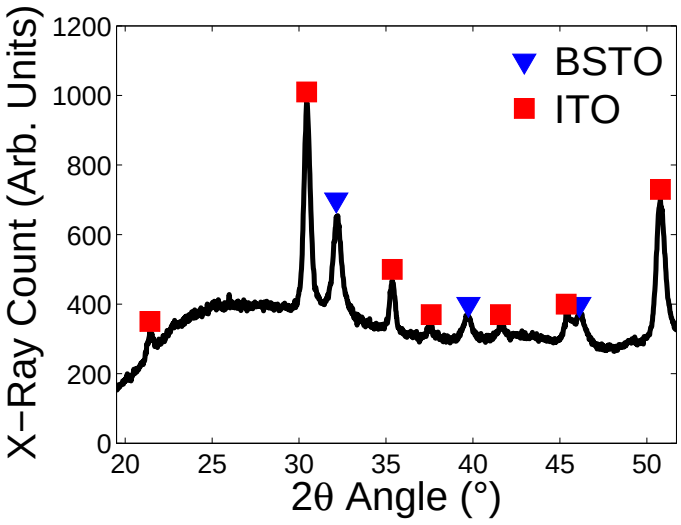

Figure 4.23: XRD Patterns of BSTO on ITO coated silica

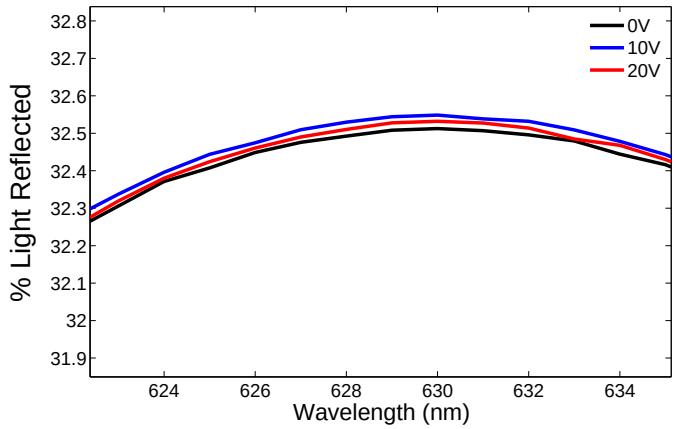

Figure 4.24: Spectrometer Measurement of BSTO on ITO coated silica

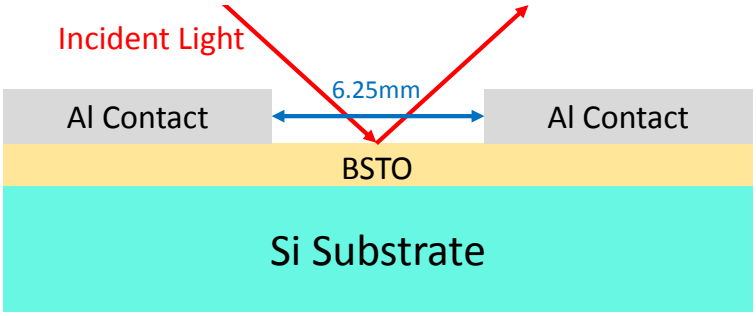

Figure 4.25: Diagram of process used to measure BSTO index by spectroscopic ellipsometry

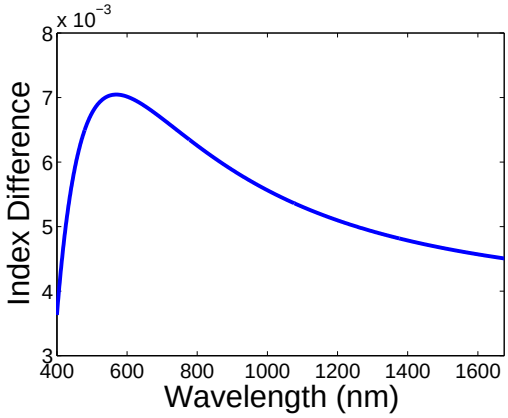

(a) Difference in Index between Sample without applied voltage and sample with applied voltage

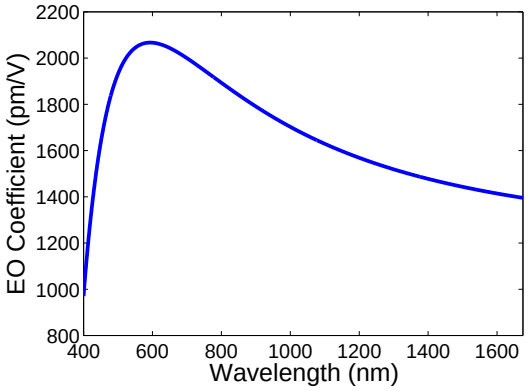

(b) EO coefficient in BSTO films.

Figure 4.26: Results of EO measurements of BSTO films

tures which had the electric field going through the film and the substrate, this structure was engineered to ensure the BSTO layer will absorb most of the electric field. The ellipsometer will then measure between the two electrodes to measure a possible index change. The difference between the measurement with and without an applied voltage is shown in figure 4.26a. This is about a 0.1% change in the index of the film. Calculating the EO coefficient from equation 4.3 and accounting for a piezoelectric contribution of 26pm/V[33] results in a very high EO coefficient, shown in figure 4.26b, which has a maximum value of 2067pm/V, which is extremely large for a polycrystalline film.

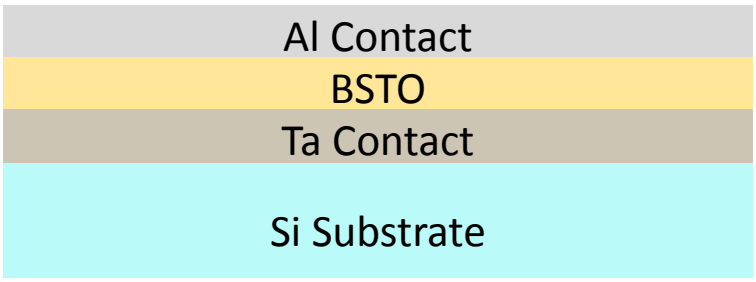

Figure 4.27: BSTO on Ta film for Fabry-Perot resonator

4.12.4 Second Fabry-Perot on Si

Although the method described in section 4.12.3 was successful in detecting an EO effect, it might be possible to induce even more of an effect with a greater electric field. A proposed design to accomplish this is shown in figure 4.27. This is essentially another Fabry-Perot structure, but unlike previous designs, in this configuration, all of the electric field and light is confined within the BSTO film. This is achieved by making the bottom contact of the structure out of tantalum, then depositing BSTO onto it. Ta is a metal with a melting point of 3020^{o}C, so it would be able to be used during the annealing process. In fact, Ta is sometimes used in epitaxial processes because of its ability to withstand high temperatures. Because of this, BSTO could be deposited and annealed without damaging the Ta layer, then a second Al contact would be deposited on top of that, creating a Fabry-Perot resonator that does not have to pass through the substrate. Although this structure was never actually fabricated, it has the potential to be a useful way to measure the EO effect because it does not require light to pass through eh substrate and allows for application of a very high electric field to the BSTO layer. If this structure were to be used with a 100nm thick film of BSTO from section 4.12.3 with a 10V bias, the amount of index change in the film would be $\Delta n = -.103$ compared to the $\Delta n = -.002$ of section 4.12.3.

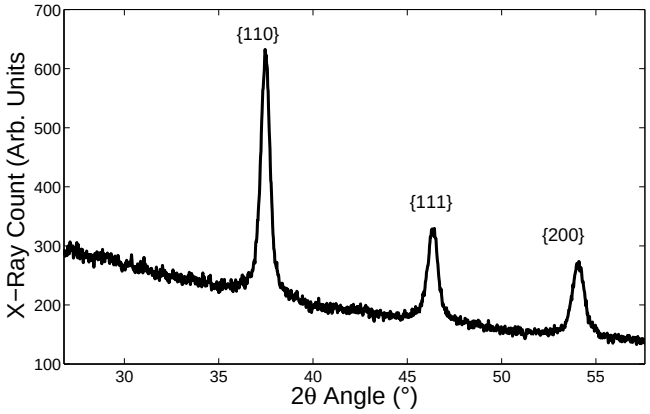

Figure 4.28: XRD Pattern of BSTO films after exposure to neutrons

4.13 Effects of Radiation on BSTO

As discussed in section 4.3 One of the reasons for pursuing BSTO as an alternative to lead-based perovskites is the fact that it does not contain lead, and would be advantageous in high-radiation environments. To test the rad-hardness, the BSTO films from section 4.11 were exposed to a flux of 5 * 10^{12} protons/cm^{2}at an energy of 217MeV to investigate for changes to any of their properties. Figure 4.28 shows the XRD pattern of these films after exposure, which remains unchanged. Additionally, the dielectric constant increases with exposure to radiation. The blue curve of figure 4.18 shows the impedance of the sample after radiation exposure, which has doubled. This is likely due to the breakdown of the crystal structure into smaller grains, as smaller grain sizes result in higher dielectric constants[34]. Exposure to radiation may also increase the nucleation of defects which would increase the dielectric constant. These values for dielectric constant are similar to other BSTO films among the literature.

4.14 Waveguide Fabrication

With the discovery of ultra-high EO BSTO films, it is necessary to guide light through them and the be able to test their performance in waveguide devices. The following sections of

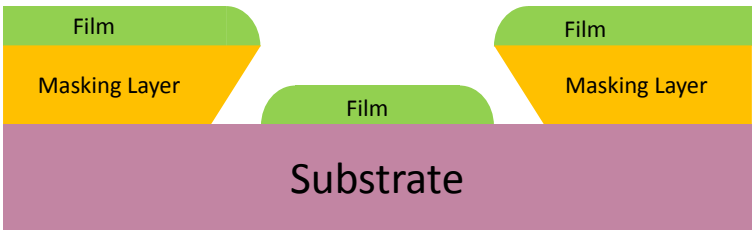

Figure 4.29: Diagram of Liftoff Method. Overhang of masking layer allows the film to lift off without rough edges

this chapter discuss the use of BSTO to construct photonic devices.

4.14.1 The Liftoff method

In order to guide light through BSTO, it must first be patterned into a waveguide. As has been previously demonstrated in section 3.20 on YIG waveguides, there is a tendency to form rough edges as a result of the etching process. The lift-off process is used to avoid this problem. A diagram of the result is shown in figure 4.29. Because the masking layer has a slight overhang, the deposited material does not coat onto the sidewalls of the masking layer. This means that the deposited material does not break off when the mask is removed. This results in a smooth waveguide pattern with no rough edges.

Originally, this procedure has been performed by using chlorobenzene to as a mask hardener. After a photoresist layer is patterned by photolithography, the sample is soaked in chlorobenzene, which causes the photoresist to harden at the surface, so when it is developed, it etches selectively, and an undercut is made resulting in the overhang profile necessary for liftoff. This procedure is not used very much anymore due to the toxicity of chlorobenzene.

The modern method to perform liftoff is to use lift-off-resist (LOR). LOR is a resist that is not photosensitive, and is developed using a different developer solution than photoresist. This allows it to be used as a second layer along with photoresist to produce an overhang.

The LOR processes requires two layers to be be deposited. The first step is to first deposit LOR and then photoresist in two layers then pattern the photoresist by conventional

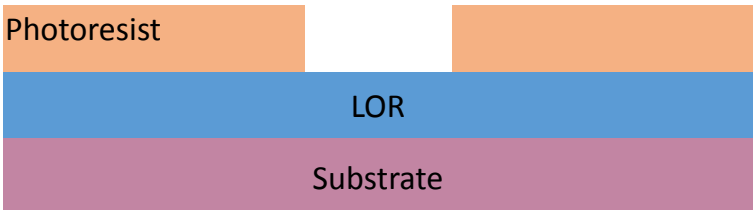

Figure 4.30: Patterning of photoresist and LOR layer

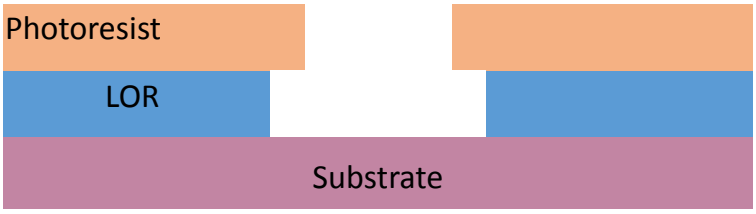

Figure 4.31: LOR After development results in undercut

photolithography. Because the two layers are soluble in different developer solutions, the photoresist will develop but the LOR will not, resulting in the structure shown in figure 4.30. After this is complete, a second development is performed using the LOR developer. The LOR then dissolves selectively, forming an undercut underneath the photoresist layer as shown in figure 4.31. After this is complete, a film can be deposited and lifted off resulting in clean edges.

4.14.2 Lift-off-Resist on Sapphire

The LOR process requires several different hotplate baking steps, and for most materials, this is not a challenge. The substrate of choice for BSTO films, however, is sapphire, which requires extraordinary considerations to perform the LOR process because sapphire is very susceptible to heat shock. Below is the process used to get an LOR pattern onto sapphire.

1. Place the wafer onto a hotplate at room temperature. Heat the hotplate to 200^{o}C then set the hotplate back to room temperature and allow it to cool. This is is to dehydrate the wafer. For all steps, do not remove the wafer until it has cooled, or it will crack.

2. Spin coat wafer by gradually increasing spin speed to 3000rpm at a slow rate.Start the spinning at 500rpm for a few seconds prior to ramping up to 3000rpm.

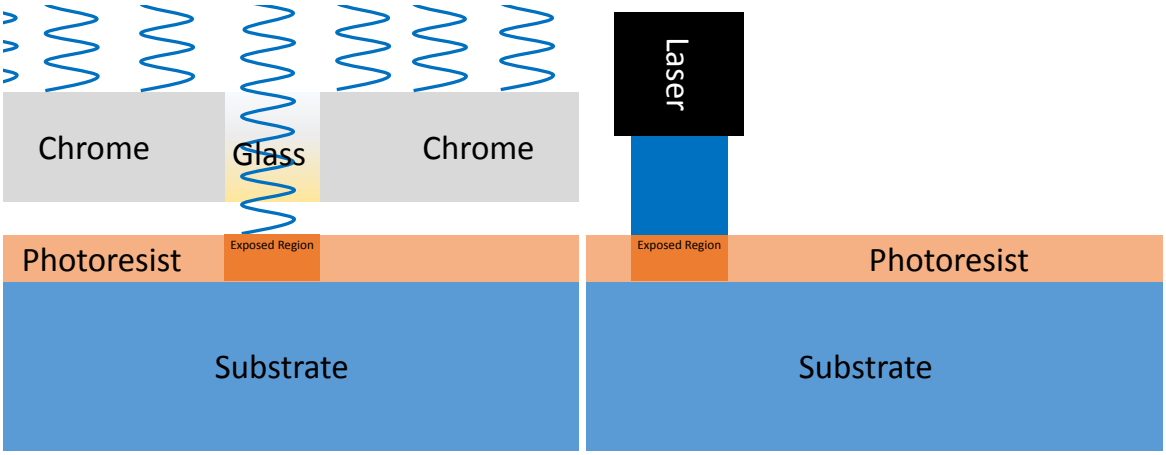

(a) Photolithography using contact alignment (b) Direct Laser Writing Photolithography

Figure 4.32: Photolithography Processes

3. Place wafer on hot plate and set for 170°C, then set it back to room temperature and allow it to cool.

4. Spin coat photoresist layer and perform photolithography. It is best to use a very thin coat of photoresist, approximately 200nm is sufficient. Develop photoresist

5. Place wafer on hot plate and set for 150°C, then set it back to room temperature and allow it to cool. This is an essential step because it hard bakes the photoresist. If the photoresist is not hard baked, it will come off during LOR development

6. Develop LOR with CD-26 solution. This development takes about 30 seconds.

4.14.3 Direct Laser Write Photolithography

The conventional method to perform photolihography has been to use a mask to block the UV light. A mask is a sheet of glass coated with chrome in the places where the UV light is to be blocked. The process is shown in figure 4.32a in which the light is blocked by the mask, and only regions where there is no chrome are exposed and developed.

An alternative method to using masks is to use direct laser writing. In direct laser writing, a focused UV laser is scanned over the the surface of the wafer and writes the

pattern directly into the photoresist as shown in figure 4.32b. The photoresist coating and development process steps for using laser writing are exactly the same as with other forms of photolithography. The only difference is the use of a laser to expose the pattern. There are several advantages of using direct laser writing. One advantage is flexibility of the process. Using dark-field or bright-field exposure is controlled within software rather than having to make new masks. Also, finer patterns are possible with laser writing, down to approximately 1μm as opposed to about 20μm when using masks. However, laser writing is slower than using masks, especially for multiple samples, so for large volumes of wafers where micron-scale precision is not needed, masks are a superior option.

4.14.4 Varying Waveguide Sizes

Previous work from [26] had demonstrated that when high film stress is present, it is possible to reduce film stress by patterning waveguides prior to annealing to reduces the surface area of the film and prevent cracking as shown in section 3.4.2. Waveguides were fabricated using the process from section 4.14.2 with varying thicknesses from 2μm to 20μm. Waveguides of 2μm thickness are shown in figure 4.33 which did not crack. The largest waveguides not to crack were the 8μm waveguides shown in figure 4.34. Waveguides larger than 8μm, such as those shown in figure 4.35, would crack during the RTA step.

4.15 Sawing and Polishing

For butt-coupling, the edges of the waveguides must be very smooth. Several methods were attempted to polish film edges for optical transmission.

The University of Minnesota Nano Center has a DISCO 2D/6HT wafer saw to cut substrates. This can cut wafers up to 1mm thick and can cut non-toxic substrate materials including silicon, silica, and sapphire. This was effective at cutting samples but left rough edges, as shown in figure 4.36. These edges will not couple light into the waveguide. It

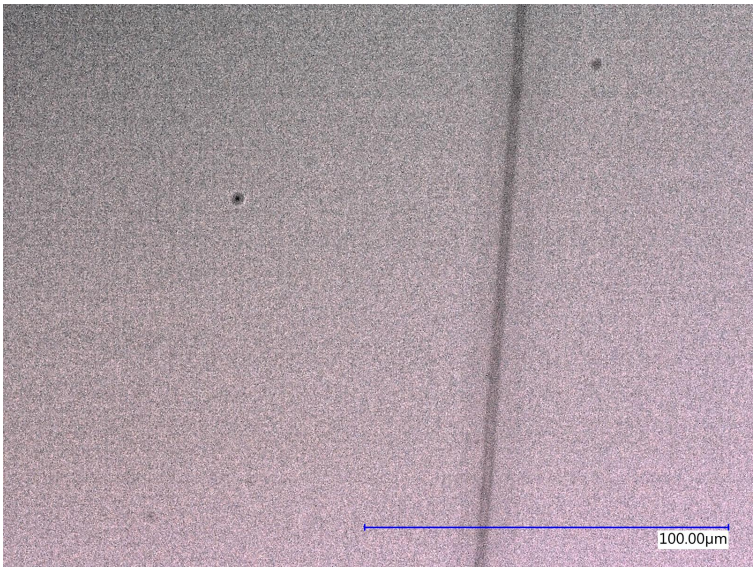

Figure 4.33: 2μm BSTO waveguides

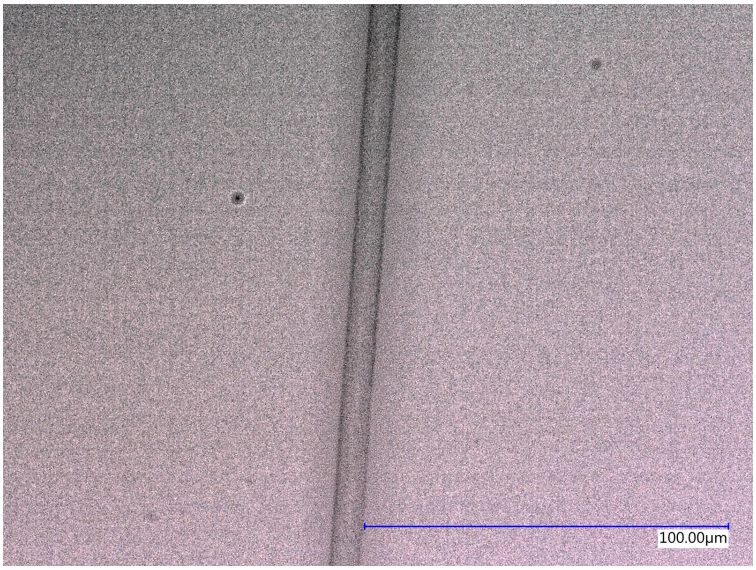

Figure 4.34: 8μm BSTO waveguides

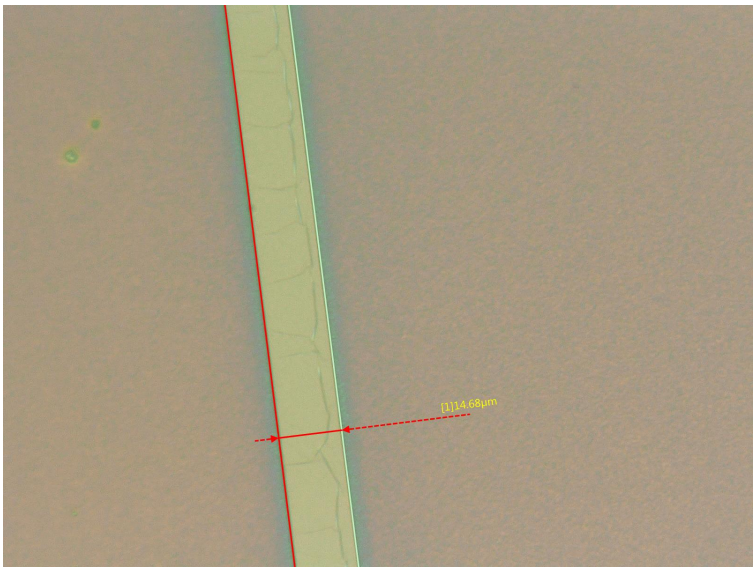

Figure 4.35: 14μm BSTO waveguide

is possible, to only partially cut a wafer, then crack the wafer at the weak point, which should result in a clean edge. This method was attempted, but when using the wafer saw, the sample is mounted on tape to secure it. This tape will peel the film from the substrate. It was then attempted to partially cut the wafer prior to any other process steps including the BSTO deposition. This was found to be ineffective as wafers would crack along the saw lines during the photolithography process due to thermal shock from the hotplate bake steps or simply from impact during transport.

The process that was the most effective in cutting the wafer was to mount the sample in an epoxy resin, cut it with a rotary saw, and polish its edges. At first, the wafer was cut prior to embedding it into the resin, but it was soon realized that the wafer and resin could be cut simultaneously resulting in a much cleaner edge. The best process to perform sawing and polishing is as follows.

1. The wafer should be cleaved to a size that will allow it to fit into the 1” mold.

2. Place the sample into the mold so that the sample is vertical and supported with plastic sample clips.

3. Mix resin according to directions and fill the mold. The sample will sit inside the

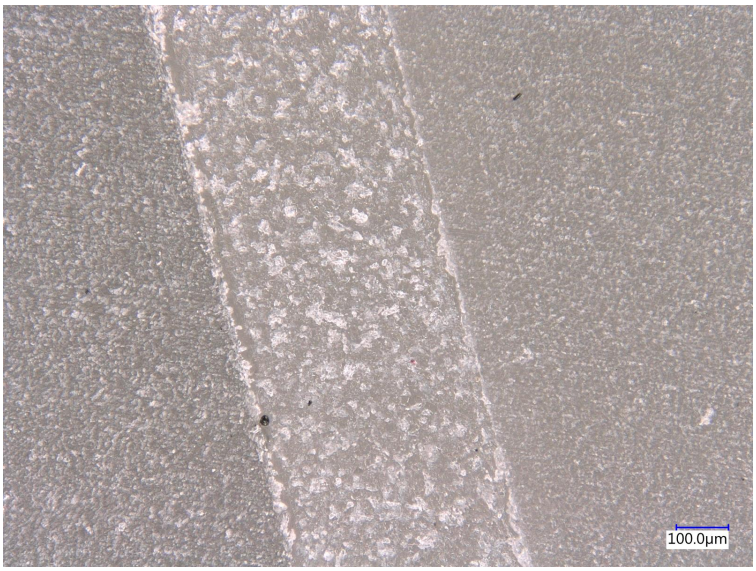

Figure 4.36: Image of side of sapphire wafer after sawing. Edges are very rough and unfit for optical transmission

resin as shown in figure 4.37.

4. After the resin cures (approximately 24 hours) remove it from the mold, and cut the resin and sample together with a circular diamond saw (located in the University characterization facility). The sample will then look like that of figure 4.36.

5. Polish the edge of the sample with diamond paper. Start with 15μm grit size, then reduce to 6μm, then 3μm, then .01μm grit diamond paper. Each polish step should be about 5 minutes. After polishing, the surface will be smooth like that shown in figure 4.38.

6. Extract the sample using heated epoxy dissolver. The epoxy dissolver can be reused until it becomes ineffective.

4.16 Waveguide Transmission Characterization

Waveguides were fabricated and characterized to determine if they were capable of supporting a guided mode. To accomplish this, 8μm wide waveguides were fabricated on

Figure 4.37: Sample Embedded in epoxy inside silicone mold

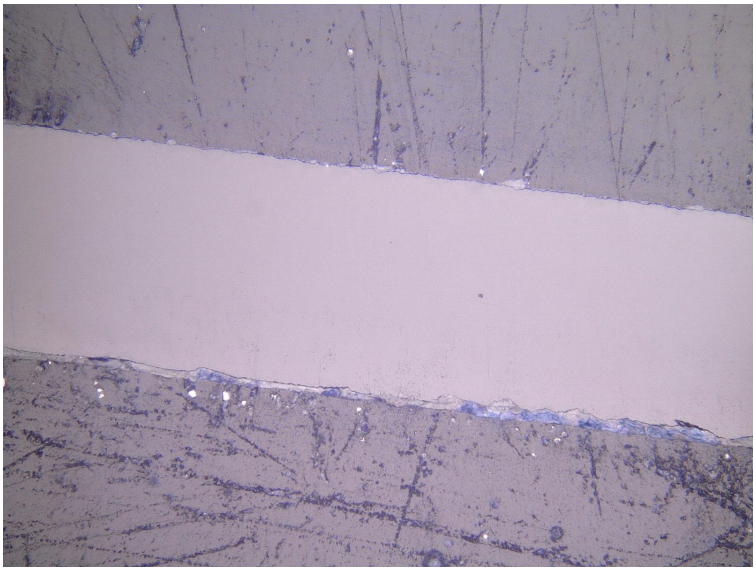

Figure 4.38: Sample edge after polishing

Figure 4.39: Waveguides used for characterization of optical transmission

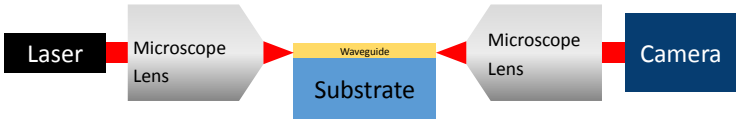

Figure 4.40: Diagram of apparatus used to characterize transmission in BSTO waveguides

sapphire substrates at a separation of 200μm using the procedures from sections 4.14 and 4.15. The waveguides are shown in figure 4.39. These waveguides were then characterized for their transmission properties using the apparatus shown in figure 4.40. Light comes from a laser, then is focused into the waveguide by a microscope lens, then after passing through the waveguide, it goes through another lens which produces an image of the guided mode at the exiting edge of the waveguide. The image is then sent to an infrared camera for viewing. Using this arrangement, a light was coupled into the waveguides, and an image was collected in the camera. As the sample was moved from side to side, the the light into the camera would grow brighter and weaker as light would couple into each waveguide. This demonstrates that these waveguides are effective at guiding light and have very high transmission.

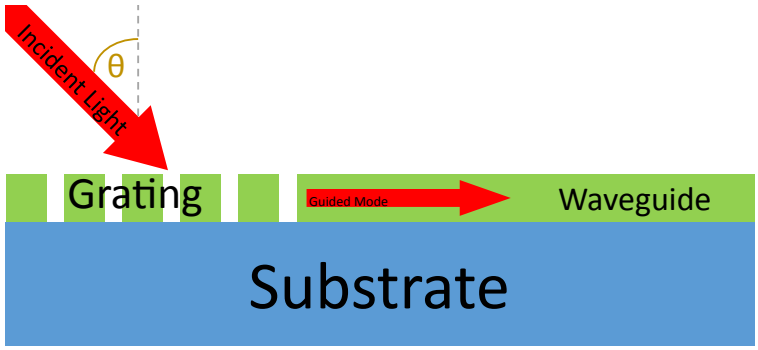

Figure 4.41: Diagram of Grating Coupler

4.17 Grating Couplers

In addition to the butt-coupling procedure from section 4.40, grating couplers were attempted to couple light into waveguides. A grating coupler, shown in the diagram of figure 4.41, is a grating built into a waveguide, where incident light is put into the waveguide at angle θ, and if the effective period of the incident matches that of the grating, light will couple into the waveguide through the grating according to the formula $n_2 k_0 \cos\theta + 2\pi q/\Lambda = \beta_m$ where n_2 is the index of the waveguide material, k_0 is the fundamental spatial frequency of the light, Λ is the period of the grating, q is a multiplier for the coupling of higher order modes into the waveguide, and β_m is the angular spatial frequency of the guided mode[19]. The minimum resolution of the laser writer from section 4.14.3 is 1μm, so the grating period was set to 2μm with a 2μm spacing. Lumerical FDTD simulations showed that the effective index of the guided mode was 1.8, therefore the incident angle θ of the grating coupler would be 116^{o}. Gratings were also designed to be 4μm and 6μm to attempt couple higher order modes in the waveguide.

4.17.1 Grating Coupler Simulations

Prior to fabricating waveguides, simulations were performed using Lumerical FDTD to confirm that they would be able to couple light. Contained in the simulations was a sapphire substrate with a 500nm-thick BSTO film, with a load layer either of SiO_2, Si_3N_4, or ZnO

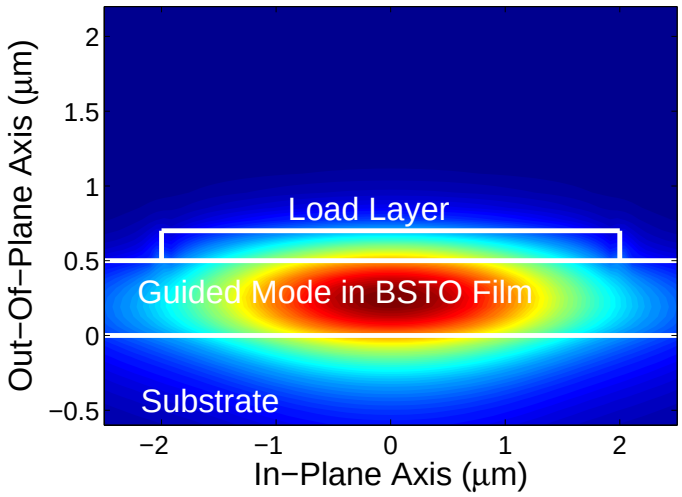

Figure 4.42: BSTO film on sapphire substrate with a Si_3N_4 load layer.

on top. A cross section of an example of the structure is shown in figure 4.42 for Si_3N_4. This demonstrates that the structure can support a guided mode. Figure 4.43 shows light coupling out of a grating coupler with a 2μ spacing and a ZnO load layer. ZnO is a highly transparent material and when deposited by ALD it has a refractive index of 1.99, slightly less than that of BSTO. This will allow ZnO to be used as an effective load layer for waveguiding.A substantial portion of the light couples out at a distance of 1μm away from the surface of the waveguide. Since light will couple out of the waveguide, it will also couple back in at the same angle. This demonstrates the feasibility of grating couplers for coupling light into a waveguide.

4.17.2 Grating Coupler Fabrication

To fabricate grating couplers, BSTO films were deposited onto sapphire substrates, then 50nm ZnO films were deposited onto the BSTO layer by ALD. Silica was also attempted using PECVD but the film was insufficiently dense and would not adhere to the BSTO layer, resulting in the PECVD film peeling off during photolithography, shown in figure4.44. After the ALD of ZnO, the films were patterned by photolithography and etched into waveguides. At first, RIE was used to etch the waveguides, but resulted in large pits in the film

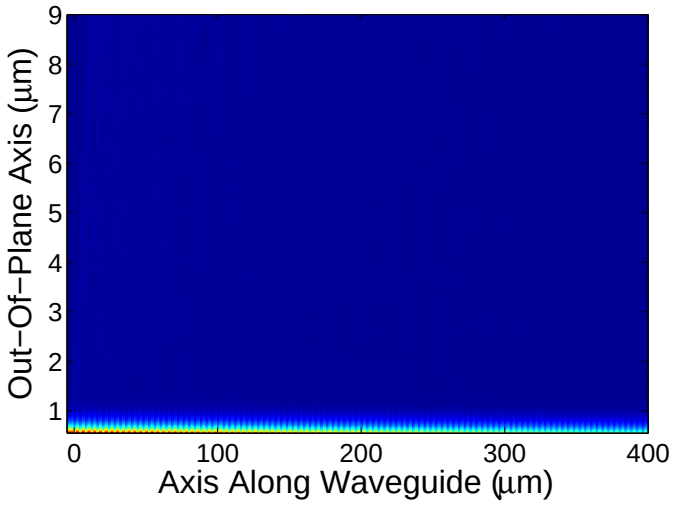

Figure 4.43: Light Coupling out of a waveguide with a ZnO load layer

as shown in figure 4.45. For this reason, buffered oxide etchant of 10% HF was used, and was effective at producing clean load layers. The final grating couplers are shown in figure 4.46. The 2μm gratings were too small to successfully etch,but the 4μm and 6μm grating formed into grating couplers.

4.17.3 Coupling light and 3D printing

After fabrication of the grating couplers was completed, a method was developed to couple light into them. The apparatus for coupling light consisted of a rotating arm with an optical fiber attached to it on a rotating stage. This allowed free rotation of the fiber to reach the coupling angle of the grating. The motion arm is shown in figure 4.47 and was produced by 3D printing. Unfortunately, it was not possible to get the fiber close enough to the waveguide to be used for coupling. The simulations from section 4.17.1 demonstrated that the fiber to needed to be within a few microns of the waveguide, and this was not possible through hand adjustment. This demonstrated that butt-coupling from section 4.16 was still the best method to get light into the BSTO waveguides.

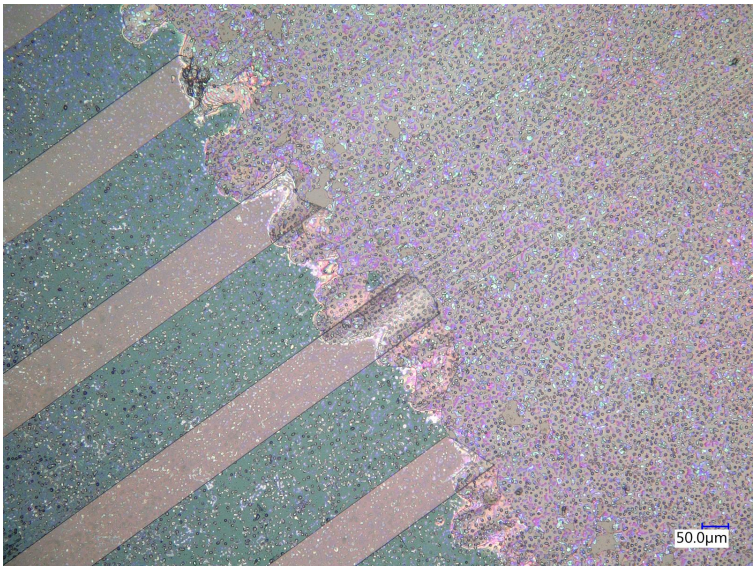

Figure 4.44: Image of BSTO film with PECVD SiO_2 deposited waveguide. SiO_2 film peeled off during photolithography processing

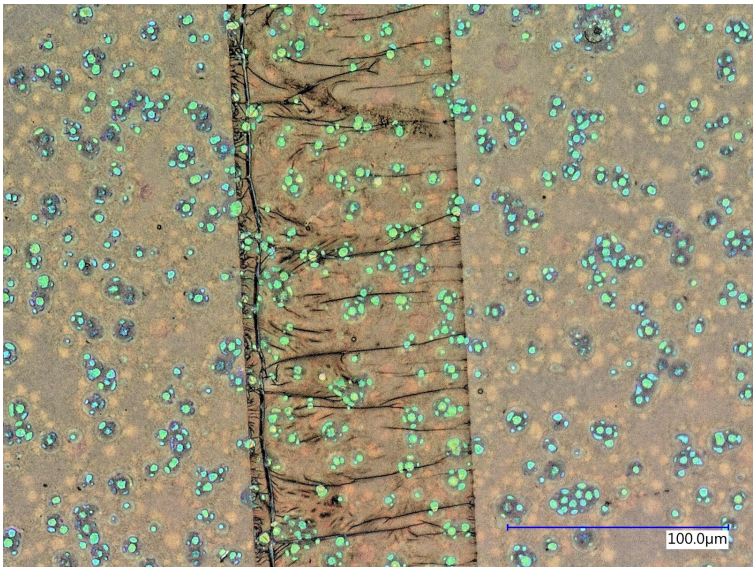

Figure 4.45: Reactive Ion Etching leads to the formation of large pits in films

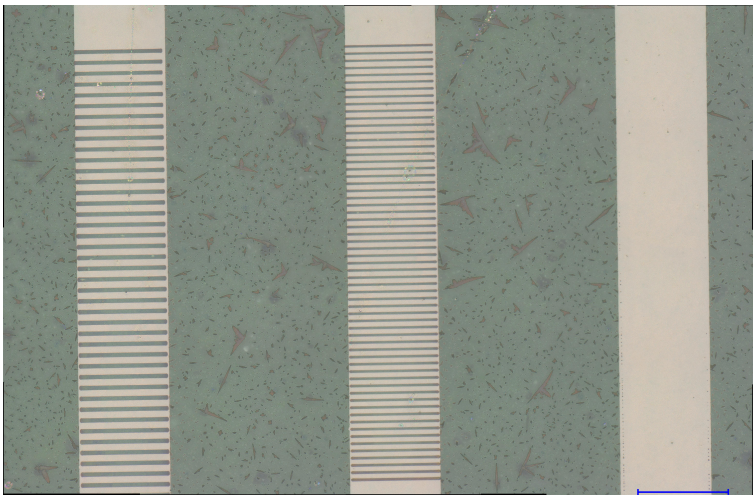

Figure 4.46: Grating couplers fabricated on BSTO films, etched by HF

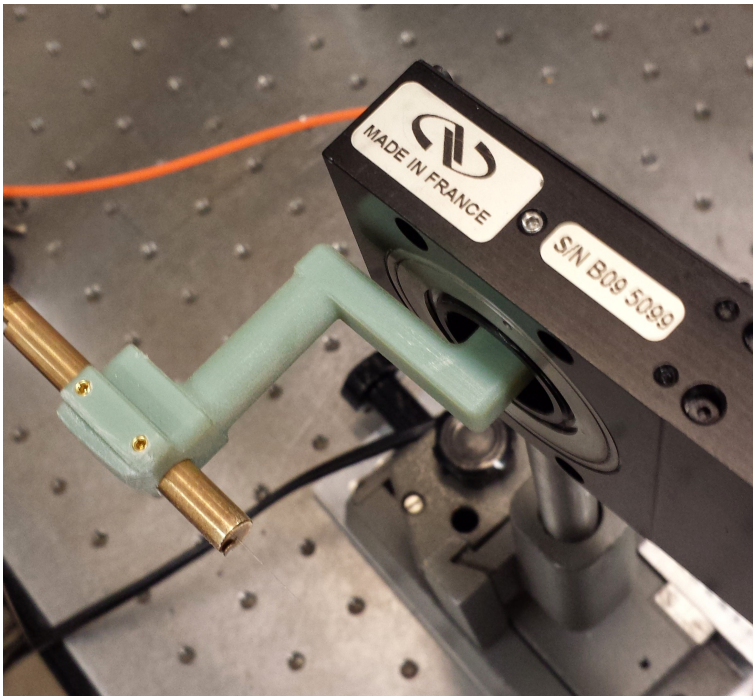

Figure 4.47: 3D printed rotation arm with attached optical fiber for grating coupling

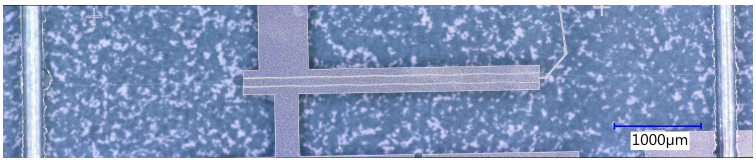

Figure 4.48: MZI device for electro-optical modulation

4.18 Future Work

All of this research demonstrates the feasibility of using BSTO as a modulator, and there is future work to be done in the actual construction and demonstration of one. A device based on a Mach-Zehnder Interferometer (MZI) was attempted to see if it was possible to construct. To make this device, A BSTO film 500nm thick was deposited onto sapphire substrates. After this, an aluminum film was deposited onto the BSTO film by evaporation. The film was then patterned using photolithography. Aluminum is advantageous to use for electrodes because it can be etched using developer solution from the photolithography process, so in order to etch it, it can simply be developed until the aluminum is etched off. After this process, a load layer of silicon oxide was deposited by PECVD, patterned, and etched by RIE. The final structure is shown in figure 4.48. The waveguide is visible branching off in two directions, then the two branches pass between the aluminum electrodes, then merge back together after being modulated. Although the device was never tested, this is a possible device configuration for use of the electro-optical effect for modulation. This device has a maximum device length of 7mm, significantly smaller than the the 3" of bulk devices, and this device would be a viable candidate for use as a modulator in small areas.

4.19 Conclusion

At the beginning of there project, there were many unknowns about the fabrication of BSTO on dielectric substrates. Was it it even possible? Could the stoichiometry be tuned? Was there an electro-optical effect? Did films have enough transparency to be used for an electro-optical device? The vast majority of these questions have been resolved. BSTO

films were made on silicon and sapphire substrates with varying stoichiometries. By tuning the stoichiometry, it was possible to fabricate a stress-free film that had very good electro-optical properties and high transparency. It was demonstrated that if made into a waveguide, these films would support a guided mode. This demonstrates that BSTO is a very good material for use in electro-optics, and that there is is good reason to explore this material in further research.

Chapter 5

Conclusion

Two complex oxides were fabricated for this thesis. The first, yttrium iron garnet, is a magneto-optical material used for the construction of isolators. The second, barium strontium titanate, is an electro-optical material used to modulate an optical signal.

The chapter covering YIG began with a discussion on its properties, and a brief history on its fabrication and integration with semiconductor materials. It then moved into a discussion on the fabrication of ultra-thin films to minimize thermal stress, and how this became a difficult task due to the incomplete crystallization of the films. A solution was discovered, allowing for the fabrication of fully crystallized YIG layers that made effective seed layers for Ce:YIG and Bi:YIG. These films were characterized using a custom-built optical test system integrating a software-based lock-in amplifier. With this system, measurements of the the magneto-optical effect showed record values for both Ce:YIG and Bi:YIG.

In addition to the work on ultra-thin films, the patterning of YIG structures was explored to determine how YIG waveguides carry light. Data from AFM was combined with computer simulations to demonstrate that YIG waveguides are highly transparent and are effective at supporting a guided mode.

The chapter concluded with a discussion on the future of YIG. It explained how new work in the areas of both films and waveguides are illuminating new information about the

formation of YIG on semiconductors. In addition, a new garnet, TIG, was discussed, that presents many new possibilities in development of non-reciprocal devices.

The chapter regarding BSTO was even more extensive than the chapter on YIG, covering not only optimizations of film performance, but the development of a new process to fabricate this material. The chapter opened with a discussion on the development of the process to create this material, and the important parameters involved and how they should be adjusted to optimize film properties. After the development of a reliable process to make these films, they were characterized by several methods to determine their stoichiometry, refractive index, dielectric constant, and electro-optical coefficient. Tests were also performed to examine the effects of ionizing radiation on BSTO.

From the work on developing films, the next step in the process was to develop a method to pattern BSTO into a waveguide. This was done using the LOR method, resulting highly transparent BSTO waveguides which were demonstrated to support a guided mode.

The conclusion of the chapter focused on the development of a BSTO modulator . From the work on BSTO waveguides, it is possible to fabricate a BSTO modulator based on a Mach-Zehnder interferometer. The feasibility of fabricating such a device was demonstrated, with future plans to characterize performance proposed for the future.

The work on both of these complex oxides represents a significant achievement for the field of photonics. Both materials have exotic properties that will be a very beneficial in working toward monolithically integrated photonic devices.

Bibliography

[1] Milton Ohring. *Materials science of thin films: deposition and structure*. Academic Press, San Diego, CA, 2nd ed edition, 2002.

[2] Optical isolator image. http://www.newport.com/Broadband-Faraday-Optical-Isolators/1041389/1033/info.aspx. Accessed: 2015-10-02.

[3] A.D. Block, P. Dulal, B.J.H. Stadler, and N.C.A. Seaton. Growth Parameters of Fully Crystallized YIG, Bi:YIG, and Ce:YIG Films With High Faraday Rotations. *IEEE Photonics Journal*, 6(1):1–8, February 2014.

[4] Optical modulator image. http://www.newport.com/High-Damage-Threshold-Phase-Modulators/917628/1033/info.aspx. Accessed: 2015-10-02.

[5] David C. Walden. Looking back at the ARPANET effort, 34 years later. *Living Internet. East Sandwich, Massachusetts: livinginternet. com. Retrieved*, 17, 2005.

[6] Smartphone users in the U.S. 2010-2018 | Forecast.

[7] How can I control how much data Netflix uses? https://help.netflix.com/en/node/87.

[8] https://www.youtube.com/yt/press/statistics.html. Statistics.

[9] *Optics and photonics: essential technologies for our nation*. National Academies Press, Washington, DC, 2013.

[10] Yurii Vlasov and others. Silicon CMOS-integrated nano-photonics for computer and data communications beyond 100g. *Communications Magazine, IEEE*, 50(2):s67–s72, 2012.

[11] D.A.B. Miller. Rationale and challenges for optical interconnects to electronic chips. *Proceedings of the IEEE*, 88(6):728–749, June 2000.

[12] Yurii Vlasov, William M. J. Green, and Fengnian Xia. High-throughput silicon nanophotonic wavelength-insensitive switch for on-chip optical networks. *Nature Photonics*, 2(4):242–246, March 2008.

[13] Joseph Thomas Verdeyen. *Laser electronics*. Prentice Hall series in solid state physical electronics. Prentice Hall, Englewood Cliffs, N.J, 3rd ed edition, 1995.

[14] L.W. Martin, Y.-H. Chu, and R. Ramesh. Advances in the growth and characterization of magnetic, ferroelectric, and multiferroic oxide thin films. *Materials Science and Engineering: R: Reports*, 68(4-6):89–133, May 2010.

[15] Ben G. Streetman and Sanjay Banerjee. *Solid state electronic devices*. Prentice Hall series in solid state physical electronics. Pearson/Prentice Hall, Upper Saddle River, N.J, 6th ed edition, 2006.

[16] Marc De Graef and Michael E. McHenry. *Structure of materials: an introduction to crystallography, diffraction, and symmetry*. Cambridge University Press, New York, second edition, fully revised and updated edition, 2012.

[17] David B. Williams and C. Barry Carter. *Transmission electron microscopy: a textbook for materials science*. Springer, New York, 2nd ed edition, 2008.

[18] Dennis Michael Sullivan. *Electromagnetic simulation using the FDTD method*. IEEE Press series on RF and microwave technology. IEEE Press, New York, 2000.

[19] Bahaa E. A. Saleh and Malvin Carl Teich. *Fundamentals of photonics*. Wiley series in pure and applied optics. Wiley Interscience, Hoboken, N.J, 2nd ed edition, 2007.

[20] Yuya Shoji and Tetsuya Mizumoto. Magneto-optical non-reciprocal devices in silicon photonics. *Science and Technology of Advanced Materials*, 15(1):014602, February 2014.

[21] Sadahiko Yamamoto and Toshio Makimoto. Circuit theory for a class of anisotropic and gyrotropic thin-film optical waveguides and design of nonreciprocal devices for integrated optics. *Journal of Applied Physics*, 45(2):882–888, 1974.

[22] Lei Bi, Juejun Hu, Peng Jiang, Dong Hun Kim, Gerald F. Dionne, Lionel C. Kimerling, and C. A. Ross. On-chip optical isolation in monolithically integrated non-reciprocal optical resonators. *Nature Photonics*, 5(12):758–762, November 2011.

[23] Ming-Chun Tien, Tetsuya Mizumoto, Paolo Pintus, Herbert Kromer, and John E. Bowers. Silicon ring isolators with bonded nonreciprocal magneto-optic garnets. *Optics express*, 19(12):11740–11745, 2011.

[24] Samir Ghosh, S. Keyvavinia, W. Van Roy, T. Mizumoto, Günther Roelkens, and Roel Baets. Ce: YIG/Silicon-on-Insulator waveguide optical isolator realized by adhesive bonding. *Optics express*, 20(2):1839–1848, 2012.

[25] Sang-Yeob Sung, Xiaoyuan Qi, and Bethanie J.H. Stadler. Integrating yttrium iron garnet onto nongarnet substrates with faster deposition rates and high reliability. *Applied Physics Letters*, 87(12):1–3, 2005.

[26] Sang-Yeob Sung, Anirudh Sharma, Andrew Block, Katherine Keuhn, and Bethanie J. H. Stadler. Magneto-optical garnet waveguides on semiconductor platforms: Magnetics, mechanics, and photonics. In *Journal of Applied Physics*, volume 109, page 07B738, University of Minnesota, 2011.

[27] Lei Bi, Juejun Hu, Gerald F. Dionne, Lionel Kimerling, and C. A. Ross. Monolithic integration of chalcogenide glass/iron garnet waveguides and resonators for on-chip nonreciprocal photonic devices. pages 794105–794105–10, San Francisco, California, USA, 2011.

[28] D. Hutchings, B. Holmes, Cui Zhang, Prabesh Dulal, A. Block, S. Sung, N. Seaton, and B. Stadler. Quasi-Phase-Matched Faraday Rotation in Semiconductor Waveguides with a Magneto-Optic Cladding for Monolithically Integrated Optical Isolators. 2013.

[29] Xue Yin Sun, Qingyang Du, Taichi Goto, Mehmet C. Onbasli, Dong Hun Kim, Nicolas M. Aimon, Juejun Hu, and Caroline A. Ross. Single-Step Deposition of Cerium-Substituted Yttrium Iron Garnet for Monolithic On-Chip Optical Isolation. *ACS Photonics*, 2(7):856–863, July 2015.

[30] J.M. Benedetto, R.A. Moore, F.B. McLean, P.S. Brody, and S.K. Dey. The effect of ionizing radiation on sol-gel ferroelectric PZT capacitors. *IEEE Transactions on Nuclear Science*, 37(6):1713–1717, December 1990.

[31] Xinhua Zhu, Jianmin Zhu, Shunhua Zhou, Zhiguo Liu, Naiben Ming, Shengguo Lu, Helen Lai-Wah Chan, and Chung-Loong Choy. Recent progress of (Ba,Sr)TiO3 thin films for tunable microwave devices. *Journal of Electronic Materials*, 32(10):1125–1134, October 2003.

[32] Glyn J. Reynolds, Martin Kratzer, Martin Dubs, Heinz Felzer, and Robert Mamazza. Sputtered Modified Barium Titanate for Thin-Film Capacitor Applications. *Materials*, 5(12):575–589, April 2012.

[33] H. Khassaf, N. Khakpash, F. Sun, N. M. Sbrockey, G. S. Tompa, T. S. Kalkur, and S. P. Alpay. Strain engineered barium strontium titanate for tunable thin film resonators. *Applied Physics Letters*, 104(20):202902, May 2014.

[34] Dipankar Ghosh, Akito Sakata, Jared Carter, Pam A. Thomas, Hyuksu Han, Juan C. Nino, and Jacob L. Jones. Domain Wall Displacement is the Origin of Superior Permittivity and Piezoelectricity in $BaTiO_3$ at Intermediate Grain Sizes. *Advanced Functional Materials*, 24(7):885–896, February 2014.

Index